Polycrystalline simulations of in-reactor deformation of recrystallized Zircaloy-4 tubes: Fast Fourier Transform computations and mean-field self-consistent model

Fabien Onimus, Lionel Gelebart, Renald Brenner

▶ **To cite this version:**

Fabien Onimus, Lionel Gelebart, Renald Brenner. Polycrystalline simulations of in-reactor deformation of recrystallized Zircaloy-4 tubes: Fast Fourier Transform computations and mean-field self-consistent model. International Journal of Plasticity, 2022, 153, pp.103272. cea-03758977

HAL Id: cea-03758977
https://cea.hal.science/cea-03758977

Submitted on 23 Sep 2022

HAL is a multi-disciplinary open access archive for the deposit and dissemination of scientific research documents, whether they are published or not. The documents may come from teaching and research institutions in France or abroad, or from public or private research centers.

L'archive ouverte pluridisciplinaire **HAL**, est destinée au dépôt et à la diffusion de documents scientifiques de niveau recherche, publiés ou non, émanant des établissements d'enseignement et de recherche français ou étrangers, des laboratoires publics ou privés.

Polycrystalline simulations of in-reactor deformation of recrystallized Zircaloy-4 tubes: Fast Fourier Transform computations and mean-field self-consistent model

F. Onimus[1], L. Gélébart[1], R. Brenner[2]

[1] *Université Paris-Saclay, CEA, Service de Recherches Métallurgiques Appliquées, 91191, Gif-sur-Yvette, France.*

[2] *Sorbonne Université, CNRS, UMR 7190, Institut Jean Le Rond d'Alembert, F-75005, Paris, France*

Abstract

Fuel cladding and structural components made of zirconium alloys, used in light and heavy water nuclear reactors, exhibit, during normal operation, significant in-reactor deformation. Fast Fourier Transform (FFT) simulations have been conducted on large grain aggregates to simulate the in-reactor behavior of recrystallized Zircaloy-4. Original constitutive equations have been proposed to account, at the microscopic scale, for thermal creep, irradiation creep and irradiation induced growth. The evolution of irradiation defects with irradiation is taken into account, especially to deduce the local growth strain. A good description of the in-reactor behavior is obtained with irradiation defects evolution consistent with Transmission Electron Microscopy observations. The FFT simulations are compared to a self-consistent model. A good agreement is obtained when the behavior is linear (irradiation creep and growth) while the nonlinear response (thermal creep) is underestimated by the self-consistent model. The FFT simulations are also compared to the lower-bound model which neglects the interactions between grains. The lower-bound model underestimates the growth strain proving the importance of using an accurate polycrystalline model to predict the growth strain from the knowledge of the irradiation defect evolution.

1-Introduction

Zirconium alloys are widely used in the nuclear industry because of their low absorption cross-section for thermal neutrons (Onimus et al., 2020b). Furthermore, thanks to alloying elements and careful microstructure control, optimized zirconium alloys exhibit a very good corrosion resistance (Allen et al., 2020; Tewari et al., 2020). They are therefore very well suited as cladding tubes or structure components in light or heavy water nuclear reactors. In the case of pressurized water reactors, these materials are used as fuel cladding tubes, for the grids of the fuel assembly and as guide-tubes of the control rods. As described in (Franklin and Adamson, 1988), in-reactor, these components exhibit significant deformation. For instance, the cladding tube exhibit a creep down toward the pellet and an axial elongation. Concerning the guide tubes, they also exhibit an axial elongation or even a bowing. These deformations are due to simultaneous neutron irradiation and complex mechanical loading. They must be well characterized and predicted for safe and efficient in-reactor operation.

Three different phenomena explain the in-reactor deformation of zirconium alloys : the thermal creep, the irradiation creep and the irradiation induced growth (Adamson et al., 2019; Carpenter et al., 1988; Fidleris, 1988; Holt, 2008; Onimus et al., 2020b; Rogerson, 1988). The thermal creep is the usual creep deformation that occurs out of irradiation. The irradiation creep is a specific deformation phenomenon which occurs under an applied stress and is activated by the fast neutron flux (Onimus

et al., 2020c). Finally, irradiation induced growth is a special deformation phenomenon since it occurs without any applied stress under fast neutron flux (Carpenter et al., 1988; Griffiths, 2020).

Several authors (Christodoulou et al., 1996; Limbäck and Andersson, 1996) have proposed empirical macroscopic models to account for in-reactor deformation of zirconium alloys. In this type of model, the polycrystalline nature of the material is not taken into account and additivity of the three irreversible strain components is assumed at the macroscopic scale. However, it was early recognized (Woo, 1985) that the polycrystalline character of the material and the interactions between grains can play a significant role on the macroscopic behavior of the material. Especially, because growth strain depends on the grain orientation, strain incompatibilities arise between the grains of the polycrystal thus inducing internal stresses that superimpose upon those due to the external load, and the local stress is relaxed by creep at the grain scale. It is through this mechanism that creep and growth couple at the polycrystal level. This is the reason why polycrystalline models have been developed and in-reactor deformation of zirconium alloys has become a textbook case for homogenization of polycrystals (Kocks et al., 1998).

Because of their industrial relevance and their significant plastic anisotropy, zirconium alloys have been an important topic of interest since the seminal work of Woo (Woo, 1985). This early paper was then followed by a large body of articles treating of deformation under irradiation of zirconium alloys, and especially irradiation creep and growth (Causey et al., 1988; Lebensohn and Tomé, 1993; Turner and Tomé, 1993; Tomé et al., 1993; Turner et al., 1994; Tomé et al., 1996; Turner et al., 1999; Tomé and Christodoulou, 2000; Patra et al., 2017; Montgomery et al., 2017).

It must be mentioned that other research teams have proposed similar approaches (Brenner et al., 2002b, 2002a) but only applied to thermal creep of zirconium alloys. Another very different, and pragmatic, approach has also been proposed for the homogenization of the behavior of polycrystals (Cailletaud, 1992; Cailletaud and Pilvin, 1994). This method has been applied to zirconium alloys after irradiation (Onimus et al., 2020a; Onimus and Béchade, 2009) but has not been applied to in-reactor deformation of zirconium alloys in the open literature.

During the last twenty years, Finite Element Method has also been used to compute the local stress and strain fields in large grain aggregates. Although this type of calculation contains a large amount of detailed information, it can be used to deduce a single property which is the overall macroscopic behavior of the grain aggregate. This method is also a homogenization method and it can be referred to as a full-field method, as opposed to a mean-field method. As the computing power increased, the number of grains in the aggregate also increased giving access to more and more accurate homogenized response of polycrystals (Barbe et al., 2001; Delannay et al., 2006; Diard et al., 2005; Erinosho and Dunne, 2015; Raabe et al., 2001; Roters et al., 2010). In the past ten years a breakthrough occurred in the field of numerical homogenization thanks to the development of Fast Fourier Transform (FFT) method applied to mechanics of continuum medium (Michel et al., 2001; Moulinec and Suquet, 1998). This is a powerful and computationally efficient method, especially when combined to massively parallel implementation, when periodic boundary conditions can be applied to the structure. Recently, several authors have used FFT simulations with crystal plasticity to predict the mechanical fields in polycrystals considering various local behaviors (Lebensohn et al., 2012; Nagra et al., 2017; Paramatmuni and Kanjarla, 2019).

The present work is really a continuation of the thorough and long lasting effort to model in-reactor deformation of zirconium alloys. Many ideas used here are inspired by the early work of Woo (Woo,

1985) followed by Turner and Tomé (Turner and Tomé, 1993), Tomé, So and Woo (Tomé et al., 1993) and Turner, Tomé and Woo (Turner et al., 1994).

Two different homogenization methods have been used, and compared, in this study. First we have used the full-field homogenization tool developed by Gélébart and coworkers (Gélébart and Mondon-Cancel, 2013; Gélébart and Ouaki, 2015; Marano et al., 2019; Marano and Gélébart, 2020) which is based on the Fast Fourier Transform method. This method has been applied, for the first time, to in-reactor deformation of zirconium alloys. Only the homogenized behavior has been considered in detail, although all the stress and strain fields are computed with this technique, as illustrated in Appendix A. Then, we have adapted and used the mean-field self-consistent polycrystalline model developed by Brenner and coworkers (Brenner et al., 2002a). The results of this self-consistent model are compared with Fast Fourier transform simulations.

Furthermore, there has been only few attempts (Griffiths et al., 1989) to relate quantitatively the irradiation induced growth to the microstructure evolution observed by Transmission Electron Microscopy (TEM) after irradiation. Correlation between <c> loop density and growth strains have remained largely qualitative (Bossis et al., 2009; Doriot et al., 2018, 2014; Yagnik et al., 2018). Several authors have proposed numerical approaches to deduce the growth strain rate from the microstructure evolution under irradiation. These numerical approaches are based on solving rate theory equations (Barashev et al., 2015) or cluster dynamics modeling (Christien and Barbu, 2009). Recently, several authors (Montgomery et al., 2017; Patra et al., 2017) have introduced these rate theory equations into a self-consistent model to deduce the growth strain at the polycrystalline scale and not only at the grain scale.

In this work, we propose an original approach to deduce the growth strain from the microstructure observed by TEM. Furthermore, we give a complete set of constitutive equations for the grain behavior, taking into account thermal creep, the effect of irradiation on thermal creep and also irradiation creep and growth. Finally, we have gathered a valuable experimental data base for recrystallized Zy-4, on which the proposed model is adjusted.

In the following section, referred to as section 2, the two homogenization methods are first presented. Then, in section 3, the material is presented and the two procedures to take into account the crystallographic texture of the material are described. In section 4, the local intra-granular behavior is presented in detail. In section 5, the experimental data base, the parameter identification and the simulation results obtained at the macroscopic scale using the FFT simulations are described. Then, in section 6, a sensitivity study of the FFT simulations is provided. Eventually, the results of the FFT simulations are compared, in section 7, with the results of the self-consistent model. Finally, the results of the simulations are discussed in section 8. The influence of irradiation creep on the growth behavior is particularly analyzed by comparing the self-consistent model with the lower-bound model.

2-Homogenization methods

2-1. Full-field homogenization using Fast Fourrier Transform method

Briefly, full-field homogenization consists of three steps: i) extraction of a subset, *i.e.* unit-cell, from a microstructural representation of the material, ii) numerical simulation of the unit-cell submitted to an applied load, iii) post-treatment of the numerical solution to determine average quantities. The quality of the result depends on both the unit-cell (size and discretization) and the boundary

conditions (BC) used in numerical simulations. Using periodic BC provides a better estimate compared to kinematic uniform or stress uniform BC (Kanit et al., 2003), leading respectively to stiff and soft estimates (upper and lower bounds in the linear case (Huet, 1990)). In that context, the FFT-based code AMITEX_FFTP ("AMITEX software," n.d.), that applies periodic BC and enables efficient and large scale simulations with its parallel implementation, is well-suited to provide reference results for comparison with self-consistent estimates. The FFT-based solver relies on the fix point algorithm (Moulinec and Suquet, 1998) accelerated with an Anderson acceleration technique (Chen et al., 2019). The discrete Green operator used in the solver is built on a finite difference approximation of differential operators (Gélébart, 2020; Willot, 2015), equivalent to linear hexaedral finite elements with reduced integration (Schneider et al., 2016).

The microstructure of the polycrystal is represented by a Voronoï tessellation built on a random uniform distribution of seeds. Voronoï cells represent grains whose crystallographic orientations must be consistent with the crystallographic texture measured experimentally. For the unit-cell definition, to avoid non-realistic grain boundaries resulting from periodic BC, the microstructure is periodized. In addition, the random orientations in the unit-cell are constrained to satisfy experimental Kearns factors, as explained in section 3.2. For the simulation, the unit-cell is discretized in cubic elements, called voxels (3D equivalent of pixels in 2D images). In order to analyse the quality of the results, the following points have been considered:

- the unit-cell size, given by the number of grains within the unit-cell (N^3) (with N=3, 5, 7, 9, 13, 17, 21 used in section 6),
- the spatial discretization, given by the average number of voxels per grain (r^3) (*i.e.* the unit-cell contains $N^3 r^3$ voxels, with r=3, 5, 7, 9 used in section 6),
- the random choice of Voronoï seeds: for a given (N^3), three random unit-cells have been generated with different grain shapes (see figure 1),
- the choice of crystallographic orientations: for a given (N^3), up to five different sampling have been used.

Finally, an extreme case with one voxel per grain has also been considered. This simple unit cell allows very efficient simulations while providing a rather precise estimate, as it will be shown in the following.

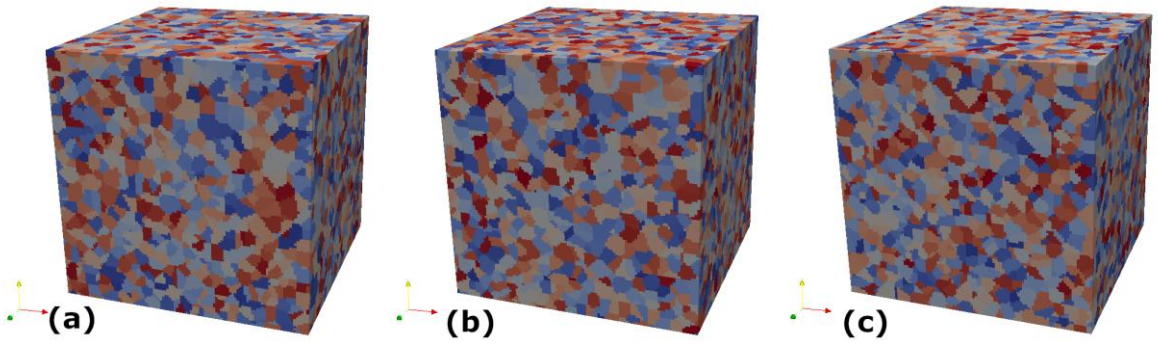

Figure 1: three random unit-cells with 21^3 grains and 5^3 voxels per grain in average (more than 10^6 voxels).

2-2. Mean-field self-consistent model

By contrast with unit-cell computations, mean-field homogenization relies on a statistical description of the microstructure and an approximate resolution of the set of field equations (constitutive equation, equilibrium and compatibility). In the case of a polycrystalline microstructure, the self-consistent model is known to provide relevant estimates for linear elastic or viscous behaviours (Lebensohn et al., 2005, 2004). It is based on the auxiliary problem of an inclusion embedded in an infinite medium. The constitutive heterogeneity, represented by the inclusion, is the crystalline orientation, or crystallographic phase.

In the present study, we have used an elasto-viscoplastic self-consistent model to simulate the transient and steady-state responses of zirconium alloys submitted to neutron irradiation and overall creep loading. The approach makes use of the correspondence principle with an efficient approximation of the inverse Laplace-Carson transform which allows to perform the resolution in the time domain (Brenner et al., 2002b). Linear (irradiation) and nonlinear (thermal) creep deformation mechanisms are considered at the local scale with an affine linearization of the thermal creep contribution (Masson and Zaoui, 1999). The irradiation growth mechanism is taken into account as an eigenstrain (stress-free strain) (Turner and Tomé, 1993). In the steady-state regime, this model is close to the widely-used VPSC model for moderate non-linearity and remains distinct from the lower-bound for high nonlinearity (Masson et al., 2000). It has been previously used to study the thermal creep of Zr-Nb-O alloys (Brenner et al., 2002a).

3-Introduction of the grain orientations or crystallographic phase orientations

3-1. Material and crystallographic texture analysis

The material studied is a zirconium alloy referred to as recrystallized Zy-4. Its chemical composition is given in Table 1.

Table 1: Chemical content (in weight %)

Sn	Fe	Cr	O	Zr
1.30	0.21	0.10-0.12	0.125-0.128	Bal.

Thin tubes are considered in this study, either guide tubes, with typical thickness of 0.4 mm and typical external diameter of 12 mm, or cladding tubes with typical thickness of 0.6 mm and typical external diameter of 9.5 mm.

First, the texture of a guide tube made of recrystallized Zy-4 has been analyzed using X-ray diffraction. The principle of sample preparation has been described in (Baron et al., 1990). The experimental data are analyzed using the Arbitrary Defined Cell method described in (Pawlik, 1986) leading to the computation of the Orientation Distribution Function (ODF). The {0002} and $\{11\bar{2}0\}$ pole figures are shown on Fig. 2. The material reference frame is defined with respect to the tube by three orthogonal directions: (1) axial direction ($\underline{u}_z$), (2) hoop direction ($\underline{u}_\theta$), (3) radial direction ($\underline{u}_r$).

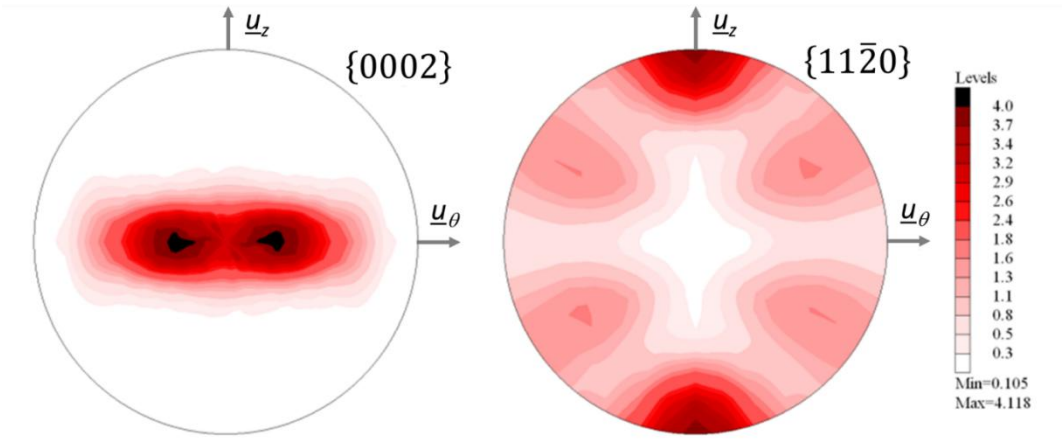

Figure 2: {0002} and $\{11\bar{2}0\}$ pole figures obtained from the XRD texture analysis of the recrystallized Zircaloy-4 guide tube.

3.2. Introduction of the crystallographic texture in the FFT simulation tool

From the computation of the ODF, it is possible, using the LaboTex software ("LABOTEX software," n.d.), to create a Single Orientation file containing an arbitrary large number of crystallographic orientations (defined by three Euler's angles) that are representative of the texture of the material. It has been chosen to use a file containing 10^5 orientations as reference file. Within this reference file, N^3 orientations, one orientation per grain of the unit cell (see section 2.2), are chosen randomly. Because the reference file contains orientations representative of the texture, a random choice of orientations extracted from this file should also be representative of the texture. However, in order to guaranty that the output file, containing only N^3 orientations, is sufficiently representative of the texture of the material, a criterion on the Kearns factor values is added to accept or reject the random choice of crystallographic orientations. The three Kearns factors, computed using the file containing 10^5 orientations are : F_{1_ref}=0.103, F_{2_ref}=0.292, F_{3_ref} =0.604 where the subscripts are 1=z, 2=θ and 3=r. The criterion used can be written, with *i*=1, 2, 3, as:

$$\mathrm{Max}\left(\left|F_i - F_{i\_ref}\right|/F_{i\_ref}\right) < 0.1\%$$

Five orientation files are selected for each N value. Simulations have been done using these five different samplings in order to check the influence of the sampling. In the following, the simulations are conducted with the sampling #1, associated to each N value, if not specified differently.

3.3 Introduction of the crystallographic texture in the mean-field self-consistent polycrystalline model

From the computation of the ODF, done using the Labotex software ("LABOTEX software," n.d.), a file containing 2527 orientations (every 10° for the 3 Euler's angles, $\varphi_1 \in [0°, 180°], \Phi \in [0°, 180°], \varphi_2 \in [0°, 60°]$) is generated. Each crystallographic orientation is defined by three Euler's angles. For each crystallographic orientation, the corresponding volume fraction is computed from the ODF value (Cho et al., 2004; Kocks et al., 1998). The Kearns factors computed from this file are the following: F_1=0.104, F_2=0.293, F_3=0.604, in very good agreement with the reference file containing 10^5 single

orientations. The two input orientation files, containing either 2527 orientations with volume fractions or 10^5 single orientations, are given in supplementary materials.

4-Intragranular constitutive behavior:

The intragranular constitutive behavior is defined, in the framework of an elasto-visco-plastic behavior, by a set of equations relating the local strain rate (either at the voxel scale, in the FFT computation, or at the crystallographic phase scale for the self-consistent model) and the applied stress. First, the total strain rate at the local scale ($\underline{\underline{\dot{\varepsilon}}}$) (the voxel scale for the FFT simulation or the considered crystallographic orientation for the self-consistent model) is the sum of the elastic strain rate ($\underline{\underline{\dot{\varepsilon}}}^e$) and the irreversible strain rate (denoted here $\underline{\underline{\dot{\varepsilon}}}^{vp}$). This last quantity includes the creep strain and the growth strain. The local elastic strain is related to the local stress by the Hooke's law ($\underline{\underline{\varepsilon}}^e = \mathbf{S}:\underline{\underline{\sigma}}$ or $\underline{\underline{\sigma}} = \mathbf{C}:\underline{\underline{\varepsilon}}^{\boldsymbol{e}}$ with $\mathbf{C}$ the anisotropic elastic moduli tensor and $\mathbf{S}$ the anisotropic elastic compliance tensor). The total local strain rate is then expressed as Eq. 1.

$$\underline{\underline{\dot{\varepsilon}}} = \mathbf{S}:\underline{\underline{\dot{\sigma}}} + \underline{\underline{\dot{\varepsilon}}}^{vp} \#(1)$$

The irreversible strain rate ($\underline{\underline{\dot{\varepsilon}}}^{vp}$) is the result of the thermal creep, irradiation creep and irradiation induced growth that occur at the local scale. It is assumed that these three phenomena are not coupled at the local scale. The irreversible strain rate can thus be written as Eq. 2, where $\underline{\underline{\dot{\varepsilon}}}^{thCreep}$ is the thermal creep strain rate, $\underline{\underline{\dot{\varepsilon}}}^{irrCreep}$ is the irradiation creep strain rate and $\underline{\underline{\dot{\varepsilon}}}^{Growth}$ is the growth strain rate.

$$\underline{\underline{\dot{\varepsilon}}}^{vp} = \underline{\underline{\dot{\varepsilon}}}^{thCreep} + \underline{\underline{\dot{\varepsilon}}}^{irrCreep} + \underline{\underline{\dot{\varepsilon}}}^{Growth} \#(2)$$

The assumption of three uncoupled phenomena is a strong approximation since at the local scale growth and irradiation creep are both the result of point defect diffusion. Furthermore, in the case of zirconium it is often considered that irradiation creep results from a dislocation climb enhanced glide phenomenon and that thermal creep results from dislocation glide. Therefore, these two phenomena are probably also coupled. It is worth mentioning that small strain is assumed for this model. In the following, the macroscopic stress and strain tensors are noted $\overline{\underline{\underline{\sigma}}}$ and $\overline{\underline{\underline{\varepsilon}}}$.

4.1 Anisotropic elasticity of zirconium single crystal

In this model, the anisotropic elasticity of zirconium single crystal is taken into account at the local scale. The elastic moduli given by Fisher and Renken (Fisher and Renken, 1964) at a temperature of 350°C are used. The moduli of the fourth order elastic stiffness tensor expressed in the usual Voigt notation are given in Table 2. The order of the index I of the C_{IJ} matrix, representing the two indices ij in the Voigt notation is ij=11, 22, 33, 23, 31, 12.

Table 2: Anisotropic elastic moduli (in GPa) for zirconium at 350°C from (Fisher and Renken, 1964).

$\boldsymbol{C_{11} = C_{22} = 127.8}$	$\boldsymbol{C_{33} = 154.3}$	$\boldsymbol{C_{44} = C_{55} = 27.6}$
$\mathbf{C_{66} = \frac{C_{11} - C_{12}}{2} = 24.25}$	$C_{13} = C_{23} = 65.8$	$C_{12} = 79.3$

4.2 Modelling of thermal creep without irradiation at grain scale

It is considered that the thermal creep behaviour is governed by dislocation glide in specific planes of the crystalline grains. This is taken into account by using classical crystal plasticity models.

The crystalline structure of zirconium is hexagonal close packed at room temperature. The lattice parameter are a =0.323 nm and c/a =1.593. There are four slip system families in the hcp lattice:

- Three prismatic slip systems for dislocations with <a> Burgers vector gliding in the $\{10\bar{1}0\}$ planes.
- Six pyramidal <a> slip systems for dislocations with <a> Burgers vector gliding in the $\{10\bar{1}1\}$ planes.
- Six basal slip systems for dislocations with <a> slip systems gliding in the $\{0001\}$ plane.
- Twelve pyramidal <c+a> slip systems for dislocations with <c+a> slip systems gliding in the $\{10\bar{1}1\}$ planes.

For each slip system, referred to with the subscript s, the constitutive behaviour must be defined with coefficients specific for each slip system family. First, it is considered, as it is usually done for classical crystal plasticity modelling, that the slip systems obey the Schmid's law (Eq. 3).

$$\tau_s = \underline{\underline{\mu_s}} : \underline{\underline{\sigma}} \#(3)$$

In this equation, $\underline{\underline{\sigma}}$ is the local stress, $\underline{\underline{\mu_s}}$ is the orientation tensor of the slip system s and τ_s is the resolved shear stress. The orientation tensor is computed as Eq. 4.

$$\underline{\underline{\mu_s}} = \frac{1}{2}\left(\underline{n_s} \otimes \underline{m_s} + \underline{m_s} \otimes \underline{n_s}\right) \#(4)$$

With $\underline{n_s}$ the normal of the considered slip system and $\underline{m_s}$ its slip direction, parallel to the Burgers vector. $\underline{n_s}$ and $\underline{m_s}$ are unit vectors.

A simple constitutive behavior is assumed for each slip system (Eq. 5). The flow rule, which relates the shear strain rate to the resolved shear stress, is a power law, with a Norton coefficient n_s and with a constant reference stress on the denominator, τ_s^c. With such a simple model, only secondary creep can be correctly modeled. A transient primary creep cannot be correctly reproduced.

$$\dot{\gamma}_s = \dot{\gamma}_0 \left(\frac{|\tau_s|}{\tau_s^c}\right)^{n_s} sign(\tau_s) \#(5)$$

Finally, from the knowledge of all the shear strain rates for each slip systems at the local scale, the overall thermal creep strain rate can be deduced from Eq. 6.

$$\underline{\underline{\dot{\varepsilon}}}^{thCreep} = \sum_s \dot{\gamma}_s \, \underline{\underline{\mu_s}} \#(6)$$

These simple constitutive equations for thermal creep have only eight adjustable coefficients: one stress exponent n_s and one reference shear stress τ_s^c for each slip system family. Associated to the reference shear stresses, an arbitrary reference shear strain rate ($\dot{\gamma}_0$) is introduced. The value of this coefficient of $\dot{\gamma}_0$=2.5× 10^{-8} s^{-1} is adopted for all systems.

4.3 Modelling of the effect of irradiation on thermal creep at grain scale

In this model, it is important to account for the radiation-induced hardening because this phenomenon decreases significantly the thermal creep strain rate. This thus leads to a reduced thermal creep under irradiation. In zirconium alloys, the radiation-induced hardening is due to the formation of numerous and small <a> dislocation loops under irradiation. These loops act as obstacles against dislocation glide. The stress required to make dislocation move is thus increased. This effect is taken into account, for each slip system, by using the classical Dispersed Barrier Hardening model. In this model, a population of loops with mean diameter d_a and number density N_a (in m^{-3}) is considered. It can be shown, using dislocation theory, that the increase in critical resolved shear stress ($\Delta\tau_c$) due to the presence of loops intersecting the dislocation glide plane is inversely proportional to the mean distance between pinning points in the glide plane (L). Since, the mean distance between loops intersecting the dislocation glide plane is related to the mean loop diameter and to the loop number density ($L = 1/\sqrt{N_a d_a}$), the increase in critical resolved shear stress is expressed as Eq. 7, where μ is the shear modulus and α is a coefficient characteristic of the strength of the interaction between dislocations and loops. This coefficient is smaller than unity. b_a is the Burgers vector of <a> dislocations and it is equal to b_a=0.323 nm.

$$\Delta\tau_c = \alpha\mu b_a \frac{1}{L} = \alpha\mu b_a\sqrt{N_a d_a} \#(7)$$

The use of the shear modulus μ assumes elastic isotropy. Because anisotropic elasticity is considered here, the effective shear modulus on a polycrystal with isotropic texture using the Voigt average procedure has been computed. In this procedure, homogeneous strain is assumed on the polycrystal (Tromans, 2011). The value obtained for the shear modulus is μ= 29157 MPa. Considering the relatively low anisotropic elasticity of zirconium this choice has only a minor impact on the results. Furthermore, this coefficient is multiplied by the coefficient α which is a fitting parameter.

Because dislocations, gliding in various planes, can be affected in different ways by the presence of loops, different values for the coefficient characteristic of the strength of the interaction (α) have been introduced for each slip system. These coefficients are noted α_s. Furthermore, we have defined the quantity ρ_a as $\rho_a = N_a d_a$ which corresponds to a linear density of dislocation loops (in m^{-2}).

In the thermal creep model, we then consider that the reference stresses, which appear in the flow law, are affected by the presence of irradiation induced loops in the same way as the critical resolved shear stress in the Dispersed Barrier Hardening model (Eq. 8).

$$\tau_s^c = \tau_s^{c0} + \alpha_s\mu b_a\sqrt{\rho_a} \#(8)$$

Under irradiation, <a> loops rapidly form and the number density and diameter saturate to typical values of 3×10^{22} m^{-3} and 7 nm (Northwood, 1977). In order to describe this evolution with fluence (φt, where φ is the mean fast neutron flux (E> 1 MeV) in $n.m^{-2}.s^{-1}$ and t the irradiation duration in s), Eq. 9 has been adopted.

$$\rho_a(\varphi, t) = \rho_a^{\infty}\left(1 - \exp(-C_3\varphi t)\right) \#(9)$$

This evolution law has only two parameters that are adjusted on the microstructural experimental data provided by Northwood et al. (Northwood, 1977). The values obtained for these coefficients are: $\rho_a^{\infty} = 2\times 10^{14}$ m^{-2} and $C_3 = 2\times 10^{-7}\times10^{-18}$ $n^{-1}.m^2$).

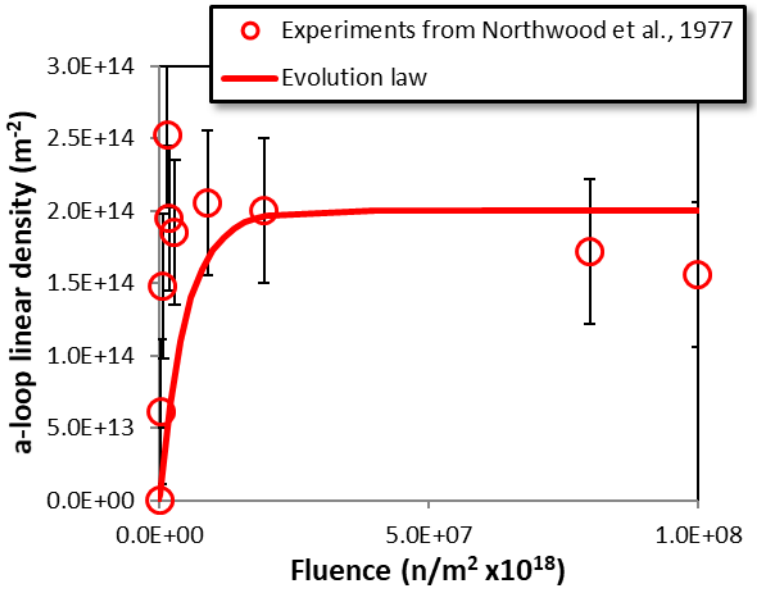

Figure 3: <a>-loop linear density evolution with fluence, from Northwood et al. (Northwood, 1977).

4.3 Modelling of irradiation creep at grain scale

It is usually considered that climb enhanced glide can explain irradiation creep of zirconium alloys. However, mass-transport mechanisms based on point defect diffusion could also play a significant role, especially when the grains are small enough. Because, irradiation creep mechanisms remain not fully understood (Onimus et al., 2020b, 2020c) we have preferred to adopt an empirical approach at the local scale, for irradiation creep deformation. Following the work of Turner et al. (Turner et al., 1999, 1994; Turner and Tomé, 1993) and Tomé et al. (Tomé et al., 1993), we have adopted a linear behavior for irradiation creep (Eq. 10). The quantity $\varphi\mathbf{k}$ corresponds to the local irradiation creep compliance tensor (with φ the fast neutron flux in n.m^{-2}.s^{-1}).

$$\underline{\underline{\dot{\varepsilon}}}^{irrCreep} = \varphi\mathbf{k}\underline{\underline{\sigma}} \#(10)$$

For the sake of simplicity, we have decided to adopt an irradiation creep compliance tensor of the same form as the one obtained by Turner et al. (Turner et al., 1999), referred to as $\mathbf{K}_{Turner}$, established for Zr-2.5Nb pressure tube material and for a fast neutron flux of φ_{Turner} =0.2×10^{18} n.m^{-2}.s^{-1}. A single proportionality coefficient, C_4, is introduced to adjust the simulated creep strain rate on the experimental behavior of the recrystallized Zy-4 (Eq. 11).

$$\underline{\underline{\dot{\varepsilon}}}^{irrCreep} = \varphi\mathbf{k}\underline{\underline{\sigma}} = C_4\frac{\varphi}{\varphi_{Turner}}\mathbf{K}_{Turner}\underline{\underline{\sigma}} \#(11)$$

The irradiation creep compliance tensor, $\mathbf{K}_{Turner}$, has only three independent coefficients, K_1, K_2 and K_3, as shown by Woo et al. (Woo, 1985) and Turner et al. (Turner et al., 1999). This tensor presents a transverse isotropy in the basal plane. It can be expressed as Eq. 12, where the fourth order is expressed in the usual Voigt notation. The order of the indices I (same for J) is the following: ij=11, 22, 33, 23, 31, 12.

$$[\mathbf{K}_{Turner}] = \begin{bmatrix} \frac{K_1}{6}+\frac{K_2}{2} & \frac{K_1}{6}-\frac{K_2}{2} & -\frac{2K_1}{6} & 0 & 0 & 0 \\ \frac{K_1}{6}-\frac{K_2}{2} & \frac{K_1}{6}+\frac{K_2}{2} & -\frac{2K_1}{6} & 0 & 0 & 0 \\ -\frac{2K_1}{6} & -\frac{2K_1}{6} & \frac{4K_1}{6} & 0 & 0 & 0 \\ 0 & 0 & 0 & \frac{K_3}{2} & 0 & 0 \\ 0 & 0 & 0 & 0 & \frac{K_3}{2} & 0 \\ 0 & 0 & 0 & 0 & 0 & \frac{K_2}{2} \end{bmatrix} \#(12)$$

The coefficients K_i are given in Table 3. Only one coefficient, C_4, remains to be adjusted on the macroscopic behavior.

Table 3: Coefficients of the irradiation creep compliance tensor.

$\boldsymbol{K_i}$	Value in $GPa^{-1}.h^{-1}$	Value in $MPa^{-1}.s^{-1}$
$\boldsymbol{K_1}$	0.32×10^{-6}	8.9×10^{-14}
$\boldsymbol{K_2}$	8.00×10^{-6}	2.2×10^{-12}
$\boldsymbol{K_3}$	3.20×10^{-6}	8.9×10^{-13}

4.4 Modelling of irradiation induced growth at grain scale

Irradiation growth of zirconium single-crystal consists of a shrinkage along the <c> axis and an elongation along the basal plane. The possible volume change (referred to as swelling) has been measured by various authors (Fidleris, 1988; Holt and Causey, 2004; Yagnik et al., 2018). This volume change is usually found to be small. In the following we assume, as it was done by Turner et al. (Turner et al., 1999, 1994; Turner and Tomé, 1993) and Tomé et al. (Tomé et al., 1993), that there is no volume change (no swelling). The growth strain tensor is therefore fully deviatoric and can be written as Eq. 13, where the two order tensor also presents a tranverse isotropy.

$$\underline{\underline{\dot{\varepsilon}}}^{Growth}(t,\varphi) = \dot{q}(t,\varphi)\begin{bmatrix} 0.5 & 0 & 0 \\ 0 & 0.5 & 0 \\ 0 & 0 & -1 \end{bmatrix} \#(13)$$

The scalar quantity $\dot{q}(t,\varphi)$ corresponds to the absolute value of the strain rate along the <c>-axis, or twice of the strain rate along the <a>-axis (Eq. 14)

$$\dot{q}(t,\varphi) = -\dot{\varepsilon}_c^{Growth} = 2\dot{\varepsilon}_a^{Growth} \#(14)$$

As described earlier the growth behaviour exhibits first a rapid transient and a stationary growth rate. Then for higher fluences, a growth acceleration or breakaway occurs. We have therefore described the growth rate as the sum of two components: one corresponding to the two first parts ($\dot{q_1}$) and one corresponding to the growth acceleration ($\dot{q_2}$) (Eq. 15).

$$\dot{q}(t,\varphi) = \dot{q_1}(t,\varphi) + \dot{q_2}(t,\varphi) \#(15)$$

4.4.1 Transient and stationary growth

The microscopic origin of the first transient and stationary growth remains not fully understood. One explanation, referred to as the Difference in Anisotropic Diffusion model (Woo, 1988), is that the diffusion of self-interstitial atoms is more rapid in the basal plane than along the <c>-axis, whereas vacancy diffusion is nearly isotropic. The highest interstitial flux toward grain boundaries perpendicular to the basal plane (with the plane normal in the basal plane) results in a positive strain in the basal plane. From the mass-balance a resulting shrinkage along the <c>-axis occurs. Then, as the interstitial and vacancy <a>-loops develop, they become the dominant sinks. The growth strain tends to saturates since the same amount of vacancy and interstitial <a>-loops has been observed. However, this model is currently being questioned since the Difference in Anisotropic Diffusion has not been proven by the latest advanced atomistic modelling method. Because there is no commonly acknowledged model, we have preferred to use a simple empirical model at the local scale (Eq. 16).

$$\dot{q_1}(t,\varphi) = \varphi A_1 C_1 \exp(-C_1 \varphi t) \#(16)$$

The coefficient C_1 is equal to the inverse of the fluence at which the growth strain saturates. The coefficient A_1 corresponds to the stationary growth strain. These two coefficients, C_1 and A_1, must be adjusted on the growth behaviour before breakaway.

4.4.2 Irradiation induced growth acceleration or breakaway

On the other hand, it has been clearly established by many authors (Fidleris, 1988; Griffiths et al., 1989; Holt and Gilbert, 1986) that the growth acceleration is associated with the appearance of <c>-component loops. However, there has been rather few attempts to quantitatively correlate the <c> loop size and density measured by TEM to the growth strain (Griffiths et al., 1989; Yagnik et al., 2018). A simple model to compute the growth strain due to the formation and growth of vacancy <c>-component loops in the basal plane of the HCP grains can be obtained by considering that the <c> loops induce a shrinkage of c/2 along the <c> axis, their Burgers vector being equal to $\frac{1}{6}\langle 20\bar{2}3\rangle$ (Christien and Barbu, 2009; Griffiths et al., 1989). Knowing the mean loop diameter d_c (in m) and the loop number density N_c (in m^{-3}), the strain along the c-axis can be computed, by using the mean-size approximation (Barashev et al., 2015), as Eq. 17.

$$\varepsilon_c^{Growth} = -\frac{c}{2}\frac{\pi d_c^2}{4} N_c \#(17)$$

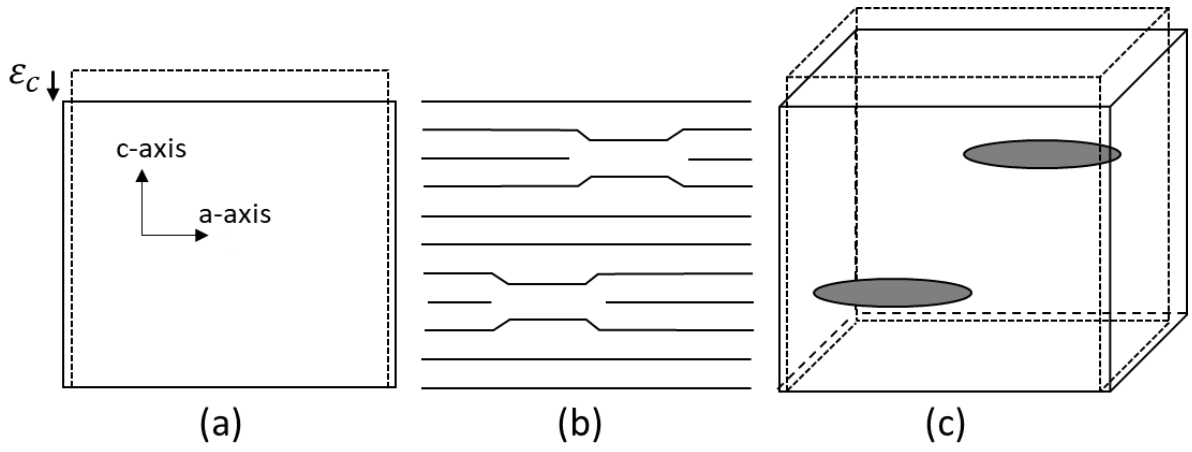

Figure 4: Schematic explaining the origin of the strain along the <c> axis during growth acceleration.

In order to account for the mass balance, if a shrinkage occurs along the c-axis, an expansion must occur along the basal plane: $\varepsilon_a^{Growth} = -\varepsilon_c^{Growth}/2$. This can either be the result of the higher growth of interstitial <a>-loops than vacancy <a>-loops, or this can be due to diffusion towards grain boundaries perpendicular to the basal plane (containing the c-axis).

Because the <c>-component loops are usually larger than the thin foil thickness (t) used for TEM observations, the loops are truncated by the foil surfaces. The diameter and number density cannot therefore be accurately measured. Instead, it is preferred to measure, on the TEM picture, the sum of the length of all segments (l_i), corresponding to <c>-loops intersection with the thin foil, observed edge-on (when the diffraction vector g=0002 is used), divided by the surface of the area studied by TEM (S) and divided by the foil thickness (t). This quantity will be referred to as L_c (in m^{-2}) and is computed as Eq. 18.

$$L_c = \frac{1}{tS}\sum l_i \#(18)$$

The relationship between this quantity measured on TEM pictures and mean loop diameter and number density can be calculated by considering a random population of <c> loops with mean diameter d_c intersecting a thin foil of thickness t, in the frame of the mean-size approximation. This relationship, derived in the Appendix C (assuming that the loop disc can always be observed even though the loop is truncated by the two surfaces of the foil), is given in Eq. 19.

$$L_c = N_c \frac{d_c}{t}\left(t + \frac{\pi d_c}{4}\right) \#(19)$$

Using this last relationship, the growth strain along the <c> axis can be computed as a function of L_c using Eq. 20 and 21.

$$\varepsilon_c^{Growth} = -k_c(t, d_c)L_c \#(20)$$

With

$$k_c(t, d_c) = \frac{c}{2}\frac{t}{\frac{4}{\pi}\frac{t}{d_c} + 1} \#(21)$$

Only few authors have measured the quantity L_c by TEM. It is Doriot et al. (Doriot et al., 2014) who give the most extensive data base for <c> loop density measurements for various zirconium alloys in PWR condition. Yagnik et al. (Yagnik et al., 2018) also provide results obtained in fast neutron material testing reactor. In the case of recrystallized Zy-4, Doriot et al. (Doriot et al., 2014) give three measurements obtained at three different fluences, starting from 9.5×10^{25} n/m^2 up to 21.1×10^{25} n/m^2. For these measurements, the thin foil thickness is considered to be t =150 nm. No value for lower fluence is provided. In order to have a more complete view of the <c> loop density evolution, we have chosen to analyze the TEM pictures provided by Griffiths et al. (Griffiths et al., 1995). These authors have observed <c> loops in recrystallized Zy-4 guide tubes irradiated in PWR at 307°C from 0.5×10^{25} n/m^2 up to 8.0×10^{25} n/m^2. The foil thickness is considered to be equal to 150 nm. The evolution of the <c> loop linear density when observed edge-on is given on Fig. 5.

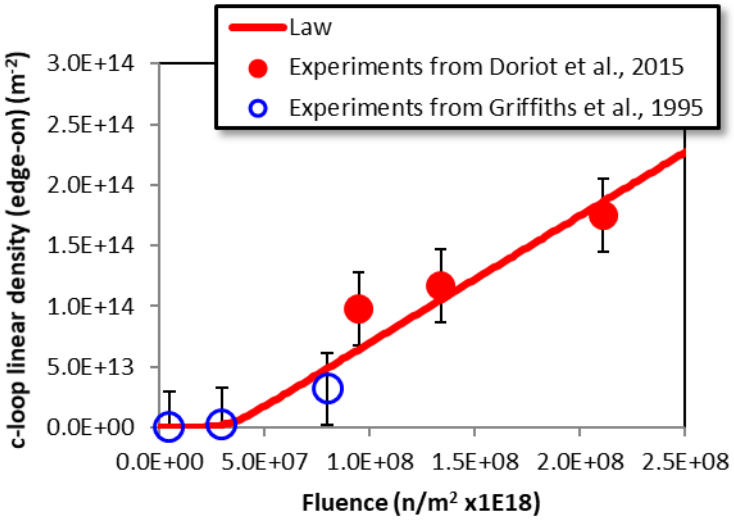

Figure 5: Experimental measurements of <c>-loop density evolution from (Doriot et al., 2018) (filled red circles) and from (Griffiths et al., 1995) (empty blue circles) and comparison with <c>-loop linear density evolution law.

An empirical evolution equation is proposed for the <c>-loop linear density (viewed edge-on), L_c (Eq. 22).

$$\frac{dL_c}{dt} = \frac{G_2 \varphi}{1 + A_2 \exp(-C_2 \varphi t)} \#(22)$$

This equation has three fitting coefficients: A_2, C_2 and G_2. The coefficient A_2 is not really a fitting coefficient since it must be high enough so that at the beginning the loop growth rate is zero. This coefficient is chosen as $A_2 = 1000$. The coefficient C_2 gives the fluence when <c> loops appear. The coefficient G_2 corresponds to the slope of the increase of <c> loop density with fluence. These two coefficients have been adjusted on the measured <c> loop density: $C_2 = 2.0 \times 10^{-7}$×10^{-18} $n^{-1}.m^2$ and $G_2 = 1.05 \times 10^{6}$×10^{-18} n^{-1}. The empirical evolution equation is plotted on Fig. 5 with the experimental values.

Once these coefficients are adjusted on the <c> loop evolution, the absolute value of the growth strain rate along the <c> axis, in the accelerated regime, can be computed thanks to the following relationship (Eq. 23).

$$\dot{q}_2 = k_c \frac{dL_c}{dt} \#(23)$$

Unfortunately, only knowing the foil thickness t and the measure of L_c is not sufficient to deduce the growth strain. A measure of the mean <c> loop diameter (d_c) is needed. This measure must be obtained thanks to additional TEM observations where the full circle of the <c> loop is observed. Griffiths et al. (Griffiths et al., 1989) show <c> loops in Zircaloy-4 irradiated at 307°C to a fluence of 8×10^{25} n/m^2 and annealed for 1 hour at 600°C. On this picture, typical <c> loop diameters range between 100 nm up to 440 nm, the mean loop diameter being around 250 nm. Harte et al. (Harte et al., 2017) also provide pictures of circular <c> loops after proton irradiation of fully recrystallized Zy-2 samples. The mean loop diameter of the loops measured on the picture is also close to 250 nm.

Recently, <c>-loops have been observed after annealing in a Zr-1%Nb-O zirconium alloy (shown in Appendix C). Large circular <c> loops are observed in that case and they have typical diameter of the order of 300 nm (200 to 350 nm depending on the method used). In the following, we have adopted a constant value of d_c =300 nm and a thickness of the foil used for the measurement of t=150 nm, leading to a value for k_c equal to $k_c = 2.36 \times 10^{-17}$ m^2. This approach is clearly simplified since under irradiation <c> loops must grow with increasing irradiation dose. Nevertheless, as explained above, this evolution has not been yet measured because of experimental limitations.

5-Data base, parameter identification and simulation results:

5.1 Mechanical tests data base

The data base used for parameters refinement comes from various sources. First, the non irradiated recrystallized Zy-4 results of long term creep tests conducted with an axial tensile applied stress or an internal pressure have been performed at CEA. Two tests have been conducted on guide-tubes samples with axial tensile applied stress of 90 MPa and 100 MPa at 350°C. The gauge length of the specimen was 82 mm. The tube was regularly removed from the machine. The axial strain was obtained by measuring at room temperature, before and after test, the length between two prints initially situated at ±20 mm from the middle of the tube. Using the same procedure, the diameter is measured, before and after test. Before testing, the initial thickness is also measured for all specimens.

One test has been conducted using a pre-pressurized tube installed in a furnace at 350°C, leading to a hoop stress of 130 MPa. The tube was 106 mm long and the prints used for axial measurements are situated at ±25 mm from the middle of the tube. The tube was regularly removed from the furnace and the diameter and the length of the tube were also measured at room temperature. From the difference between the current diameter and the initial diameter, the creep strain was computed. It should be pointed out that applying an internal pressure induces a biaxial stress state, with the axial stress equal to approximately half of the hoop stress (Onimus et al., 2020a).

Concerning the behavior after irradiation of recrystallized Zy-4, only one result has been found for creep tests done at 350°C. This mechanical test has been conducted at CEA, in hot cell on a cladding tube irradiated in power reactor up to a fluence of 0.5×10^{25} n/m^2. This tube was tested at 350°C under a hoop stress of 200 MPa. In that case the diameter was measured using extensometers all along the test allowing the measurement of the total strain.

The data concerning the creep behavior under irradiation of recrystallized Zy-4 at 350°C comes from the work of Soniak et al. (Soniak et al., 2002). These authors have conducted two irradiation creep tests under internal pressure in the CEA material testing reactors Siloé and Osiris using pre-pressurized cladding tube specimens leading to hoop stresses of 90 MPa and 120 MPa. The fast neutron (E > 1 MeV) flux was equal to $\varphi = 1.75\times10^{18}$ n/m^2. The creep samples had a length of 82.6 mm, outer diameter of 9.5 mm and wall thickness of 0.6 mm. As for the test conducted on the non-irradiated sample, the initial diameter, length and thickness are measured before irradiation and the diameter and length of the samples are regularly measured in hot-cell by taking the samples out of the reactor.

The data concerning the growth under irradiation of recrystallized Zy-4 at 350°C comes mainly from the work of Gilbon et al. (Gilbon et al., 2000) and from the work of Soniak et al. (Soniak et al., 2002) where results obtained on the same specimens brought up to higher fluences are also given.

In addition to this CEA data base, which is limited to rather low irradiation fluences, other irradiation growth tests have been used. Rogerson (Rogerson, 1988) provides growth data for recrystallized Zy-2 (with grain size of 20 µm and axial Kearns factor of 0.1) at 280°C under a neutron flux between 4.1 and 10.8×10^{17} n.m^{-2}.s^{-1} in the DIDO reactor. Garzarolli et al. (Garzarolli et al., 1989) provide growth data for recrystallized Zy-4 (grain size 7 µm, axial Kearns factor 0.046) at 295°C in a PWR under a typical neutron flux of 6 to 10×10^{17} n.m^{-2}.s^{-1}. Finally, Holt and Gilbert (Holt and Gilbert, 1986) and Griffiths et al. (Griffiths et al., 1995) provide other data obtained on guide-tubes made of recrystallized Zy-4 at temperatures ranging from 287°C to 311°C under a typical flux of 6 to 10×10^{17} n.m^{-2}.s^{-1} in PWR reactors, with similar grain size and Kearns factors.

5.1 Simulation results of thermal creep tests

First, the three tests conducted on non-irradiated specimens are simulated using the self-consistent model. For axial creep test, a uniaxial stress tensor is applied and for internal pressure tests a biaxial stress tensor is applied with the axial stress equal to half of the hoop stress ($\sigma_{rr}=0, \sigma_{\theta\theta}, \sigma_{zz}=\sigma_{\theta\theta}/2$). An automatic fitting procedure, based on the minimization of a cost function is used to obtain the best set for the eight parameters (τ_s^{c0}, n_s), the coefficient $\dot{\gamma}_0$ remaining equal to $\dot{\gamma}_0$=2.5× 10^{-8} s^{-1}. Some constraints must be added to the minimization procedure to ensure that the prismatic slip remains the easiest slip system and the pyramidal <c+a> remains the most difficult slip system. Then, the three tests are simulated using FFT calculations with few grains and a coarse spatial discretization for accelerated procedure. The reference shear stresses are then progressively manually adjusted to obtain adequate simulation of the creep strain and creep anisotropy. The number of grains and the spatial discretization is then increased. The final coefficient set is given in Table 4. The FFT simulations done with Voronoi's grains, using N^3 grains, with N=21, a refinement of r=5, with shape sampling #1 and grain orientation sampling #1, are shown, as continuous lines, on the Fig. 6. These simulations results are compared with experimental results shown as circles. The hoop strain is shown in blue and the axial strain is shown in red. It can be noticed that a good agreement is obtained between simulation and experiments, at least for this limited stress range, although the creep model used here is particularly simple. Especially, a good agreement concerning the thermal creep anisotropy and the stationary creep rate is achieved.

Table 4: Values of the coefficients of the thermal creep constitutive equations.

Slip system	n_s	τ_s^{c0} (MPa)	α_s
Prismatic	5.9	55	0.47
Pyramidal <a>	9.4	75	0.47
Basal	6.5	66	0.19
Pyramidal <c+a>	6.5	140	0.47

Table 5: Values of the coefficients used to model the effect of irradiation on the thermal creep.

Parameter	**Value**	**Unit**
b_a	0.323	nm

μ	29157	MPa
ρ_a^{∞}	2×10^{14}	m^{-2}
C_3	$2\times 10^{-7}\times 10^{-18}$	$n^{-1}.m^2$

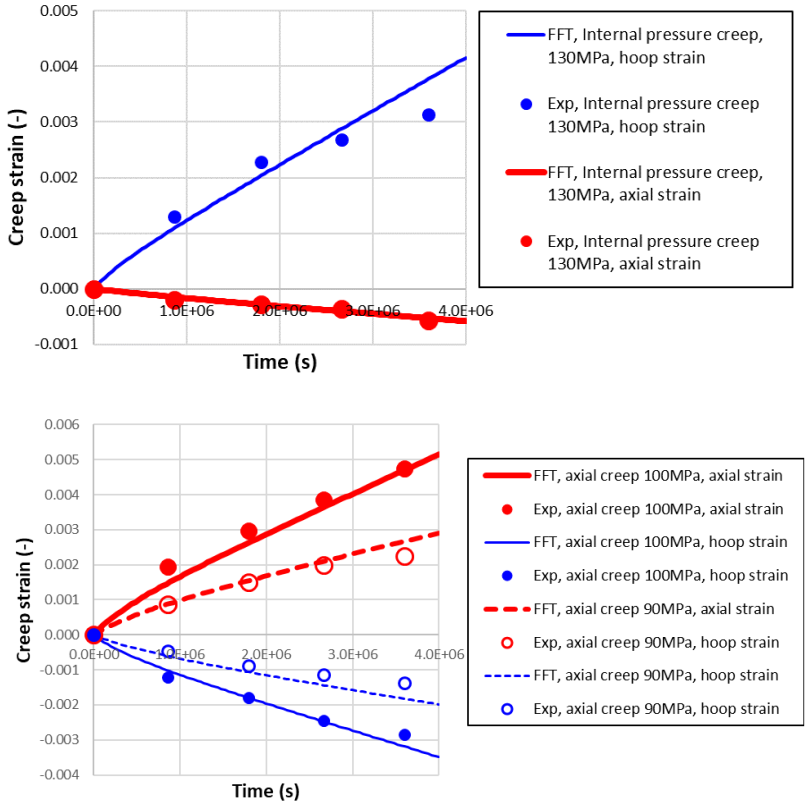

Figure 6: FFT simulations (using Voronoi grains with *N*=21, *r*=5) compared to experimental results of thermal creep tests conducted at 350°C on non-irradiated RXA Zy-4 a) with an axial applied stress of 90 MPa and 100 MPa and b) with an internal pressure leading to an applied hoop stress of 130 MPa. Both axial and hoop creep strain (total strain minus elastic strain) are plotted (in red and blue respectively).

In a second step, the parameters characteristic of the radiation induced hardening are adjusted. In order to simulate the post-irradiation creep behavior, the neutron flux is set to zero, and the <a> loop density is set at its saturation value ρ_a^{∞} . This takes into account that after irradiation the <a> loop density is high and act as obstacle against dislocation glide. However, this approach neglects the possible loop recovery during post-irradiation creep at 350°C or the possible loop clearing during dislocation glide. Then the parameters α_s are adjusted to obtain an adequate simulation of the creep test conducted with internal pressure under a hoop stress of 200 MPa. Since it has been shown that dislocations gliding in the basal planes are less pinned by loops than dislocations gliding in other planes, a coefficient α_B=0.19 has been adopted for basal slip, whereas a value of α_s=0.47 (with $s \neq B$) has been adopted for all the other three slip system families. It can be seen on Fig. 7, that a good description of the creep rate after irradiation is obtained, for this single test. The other parameters are recalled in Table 4 and 5.

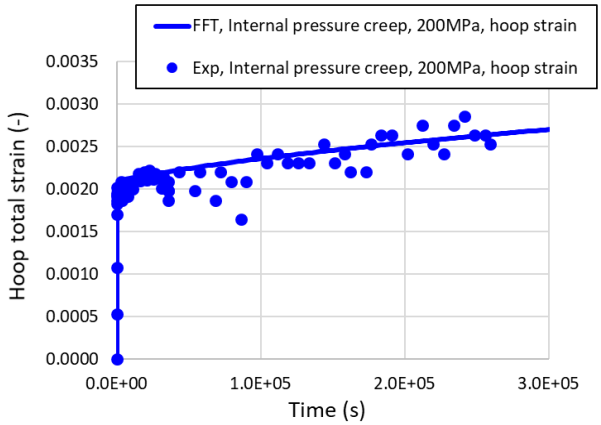

Figure 7: FFT simulations (using Voronoi grains with N=21, r=5) compared to experimental results of a post-irradiation creep test conducted at 350°C on RXA Zy-4, under internal pressure, with applied hoop stress of 200 MPa. The total hoop strain is shown as a function of time.

5.3 Simulation results of irradiation creep tests

Concerning irradiation creep, two internal pressure tests are simulated, with a hoop stress of 90 MPa and 120 MPa. The neutron flux is set at φ=1.75×10^{18} n/m^2.s^{-1}. As pointed out in (Soniak et al., 2002), the growth strain is negligible in the hoop direction. This allows a separate fitting of parameters governing irradiation creep and parameters governing growth. In this very simple approach, there is only one fitting parameter for irradiation creep (C_4). The value for this coefficient is found to be C_4=0.35, showing that the irradiation creep of recrystallized Zy-4 is significantly lower than for Zr2.5Nb pressure tube material. A correct description of stationary irradiation creep for a hoop stress of 90 MPa is obtained (Fig. 8). Furthermore, its anisotropy is also well reproduced. However the simulated creep strain for a hoop stress of 120 MPa is lower than the experimental creep strain, suggesting that the stress exponent for irradiation creep of recrystallized Zy-4 is slightly higher than unity. This was already discussed by Soniak et al. (Soniak et al., 2002) who obtained a macroscopic stress exponent of 1.43.

It is worth pointing out that the introduction of the progressive hardening of thermal creep with irradiation is not able to reproduce the primary creep observed experimentally. The primary creep observed must therefore have another origin than the progressive retarded thermal creep due to radiation hardening.

The hoop strain and hoop stress distribution in the grain aggregate computed during the simulation of the in-reactor creep with hoop stress of 90 MPa, are given in Appendix A.

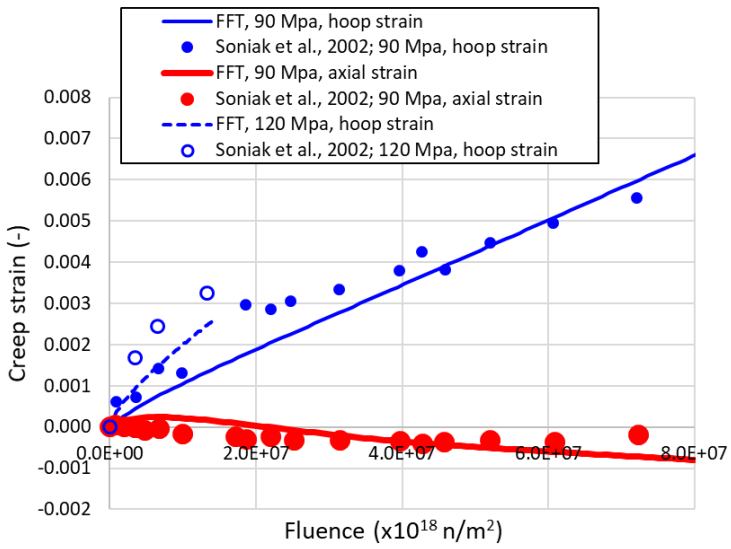

Figure 8: FFT simulations (using Voronoi grains with N=21 and r=5) compared to experimental results of internal pressure creep tests conducted on RXA Zy-4 under irradiation at 350°C in materials testing reactor (Soniak et al., 2002). Two tests are reported with an applied hoop stress respectively of 90 MPa and 120 MPa. For the test conducted with an applied hoop stress of 90 MPa, both axial and hoop strain are given (resp. in red and blue).

5.4 Simulation results of irradiation induced growth tests

Concerning irradiation growth, there are only two fitting parameters (A_1, C_1) for the first transient and stationary growth. After fitting, the coefficients obtained are A_1=1.0 × 10^{-3}, C_1=3.2 × 10^{-7}×10^{-18} $n^{-1}.m^2$. Concerning growth acceleration, there is no additional fitting parameters, since the coefficients have already been adjusted on microscopic data. The simulation results are shown on Fig. 9. A very good agreement is obtained for axial growth strain as well as for the strain along the hoop direction. From the parameters used in the model, it is interesting to plot the growth strain occurring at the local scale for recrystallized Zy-4. This is shown on Fig. 15. Furthermore, the axial strain and axial stress distribution in the grain aggregate computed during the simulation of the in-reactor creep growth, are given in Appendix A.

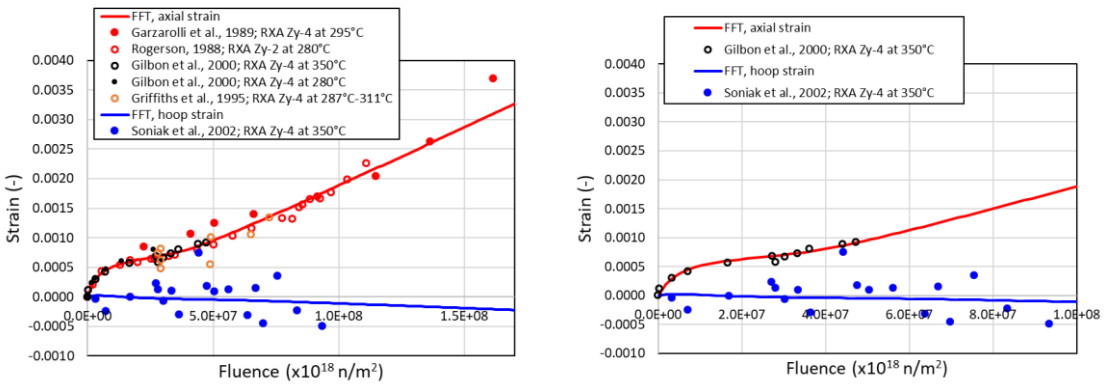

Figure 9: FFT simulations (using Voronoi grains with *N*=21 and *r*=5) of irradiation induced growth tests compared with the full experimental data base, (b) the simulation is compared with the experimental results obtained on RXA Zy-4 at 350°C provided by (Gilbon et al., 2000; Soniak et al., 2002). Soniak et al. (Gilbon et al., 2000) provide measurements of the hoop strain growth strain (in blue). Axial strain is shown in red and hoop strain is shown in blue.

To summarize, the growth model requires 6 input parameters. Some of them have been obtained from fitting on microstructure data and some of them have been deduced by fitting on the macroscopic mechanical behavior. All these parameters are recalled in Table 6.

Table 6: Parameters for the transient, stationary and accelerated growth.

Parameter	Value	Unit
A_1	1.0×10^{-3}	-
C_1	3.2×10^{-7}×10^{-18}	$n^{-1}.m^2$
A_2	1000	-
C_2	2.0×10^{-7}×10^{-18}	$n^{-1}.m^2$
G_2	1.05×10^{6}×10^{-18}	n^{-1}
k_c	2.36×10^{-17}	m^2

6. Sensitivity study of the FFT simulations

The FFT numerical simulations performed in this work are sensitive to spatial discretization, grain number, grain orientation sampling or seed choice of Voronoi's grains. In order to evaluate the influence of these choices on the numerical results, a sensitivity study has been conducted.

For this sensitivity study, only the thermal creep test on the non-irradiated material under an axial stress of 100 MPa has been computed. The total axial strain at the end of the creep test (t=4×10^6 s) has been recorded for each simulation and compared. It has been chosen to compare the total strain instead of the creep (visco-plastic) strain only, because the elasticity is heterogeneous (anisotropic elasticity at the local scale). For different choices of grain aggregates, the macroscopic elastic strain must therefore be different. Voronoi's shape grains have always been used, except when the grains contain only one voxel. In that case the grains are obviously cubic.

First, the influence of the choice of the number of grains (N^3) has been studied. Six values for N have been chosen: 3, 5, 9, 13, 17, 21. For each N value, N^3 orientations have been chosen randomly in the file containing 10^5 grains orientations representative of the texture. As described earlier, only the samplings that have the correct Kearns factors have been selected. Five different grain orientation samplings have been selected for every N value. Then, these 30 different simulations have been performed on unit-cells containing N^3 Voronoi grains with a spatial discretization always equal to r=5. The results are plotted on Fig. 10. For a small number of grains, there are significant discrepancies between the various results. As the number of grains increases the final strain tends to be the same for the various samplings. For N=21, the discrepancies are very small. This N value thus leads to a converged final strain. The average final total strain over the five different samplings ($\bar{x}$) for N=21 has been computed and the relative absolute value of the maximum deviation from this value ($Max(|x - \bar{x}|)/\bar{x}$) has been calculated for each N value. For N=3, the maximum deviation is close to 16% and it drops rapidly below 2% for N=9. For N=21 it is equal to 0.5%, showing the very low dispersion obtained for this high number of grains.

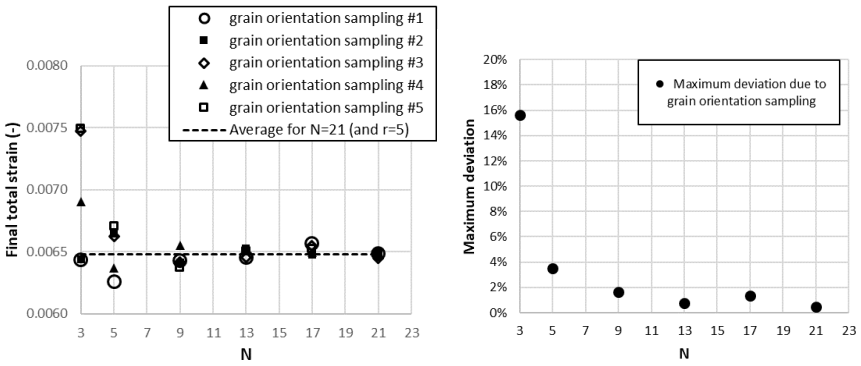

Figure 10: Sensitivity study for Voronoi grains (using a refinement parameter *r*=5), showing the influence of the grain orientation sampling and the influence of the number of grains *N*, a) on the final total strain and b) on the corresponding maximum deviation. The average on the various sampling for *N*=21 is shown.

The influence of the spatial discretization, or refinement (r), has also been studied, by choosing only N=21 (21^3 grains) and using the grain sampling #1. The refinement parameters has been increased from r=1 (cubic grains with one voxel only) to r=9 (9^3 voxels per grains, on average). Five simulations have been done (Figure 11). When the refinement parameter increases the final strain tends to slightly increase but converges to a constant value for r=9. The maximum deviation has also been computed, considering that the reference value is the converged value for r=9. For r=5, the maximum deviation is below 1% from the reference value and is therefore considered to be a good enough approximation.

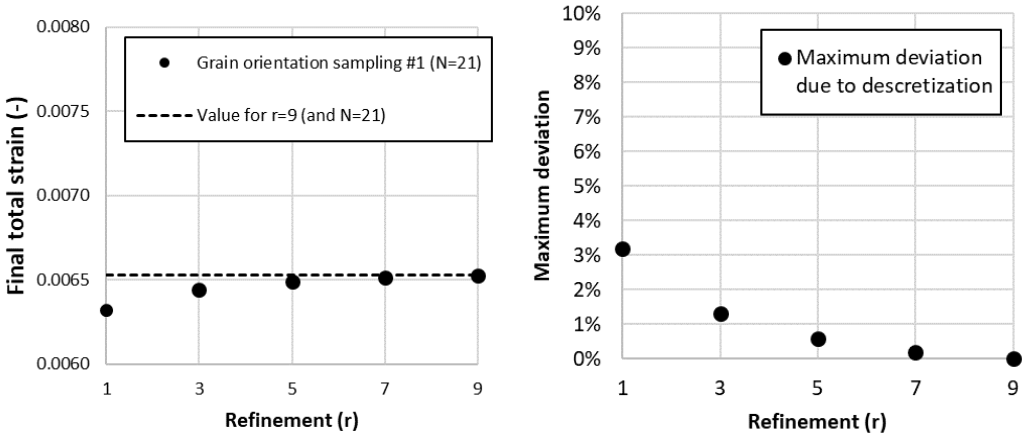

Figure 11: Sensitivity study for Voronoi grains (using *N*=21) showing the influence of the refinement parameter, *r*, (using the grain orientation sampling #1), on (a) the final strain and on (b) the corresponding maximum deviation.

Finally, the influence of the random position of the seeds of the Voronoi grains has been studied. Previously, only the grain seed sampling was tested for each grain orientation sampling. Now, only one grain-orientation sampling is used (orientation sampling #1) and three different grain seed samplings are used for each N value (Fig. 12). For the lower N value, the discrepancy between various final strain values is higher and decreases as the number of grains increases. For N=21, the three simulated final strain values are nearly the same. The average value is thus computed for N=21 and the maximum deviation from this reference value is computed for each N value. For N=5, the maximum deviation is around 3% and decreases down to 0.1% for N=21.

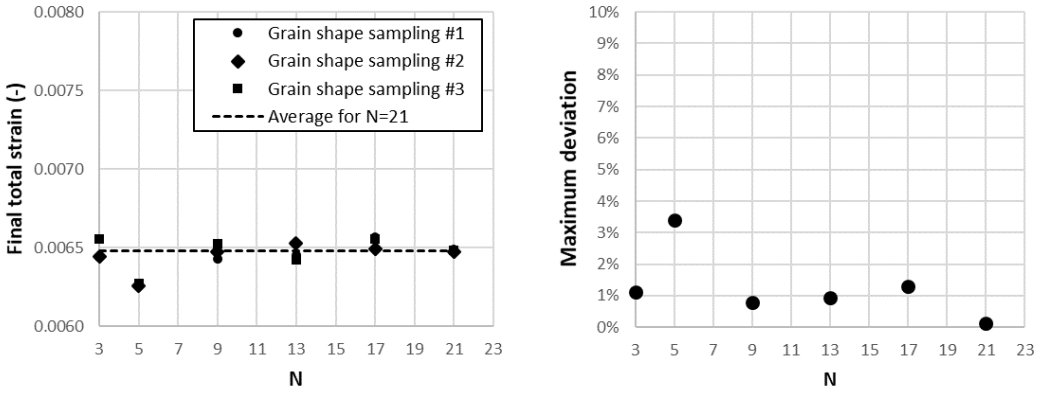

Figure 12: Sensitivity study for Voronoi shape grains, showing the influence of the sampling of the grain shape (or choice of seeds for Voronoi grains) and the influence of the number of grains (with refinement parameter *r*=5) (a) on the final total strain and (b) on the corresponding maximum deviation.

Because the maximum deviation is below 1% for grain orientation sampling and also for grain seed sampling when N=21, it is thus required to use a grain aggregate with 21^3 grains for accurate simulation. Nevertheless, a simulation with only 9^3 grains would lead to a maximum deviation of only 2%. Furthermore, to obtain accurate results it is required to use Voronoi grains with a spatial refinement equals to r=5. However, it is remarkable that a simulation with cubic grains with only one voxel per grain (r=1) leads to values only 3% away from the reference simulation (r=5) obtained on a problem size 125 times higher. Using such a simplified microstructure could allow fast computations needed for parameters fitting or even for a coupling with Finite Element method simulations of structure component.

7. Comparison with the self-consistent model

The same simulations have been conducted with the self-consistent model using the orientation file containing 2527 orientations representative of the texture of the material. For the non irradiated material, the internal pressure test with 130 MPa hoop stress and the axial creep with 100 MPa axial stress have been simulated and compared with the FFT simulations conducted with N=21 and r=5 (Fig. 13). The strain simulated with the self-consistent model is systematically lower than the strain obtained from FFT simulations. The relative discrepancy between the self-consistent model and the FFT simulations are respectively 14% and 19%, for internal pressure test and axial test, when comparing the total strain (at $t=4\times10^6$ s). This discrepancy increases up to 19% and 24% when comparing the creep strain only.

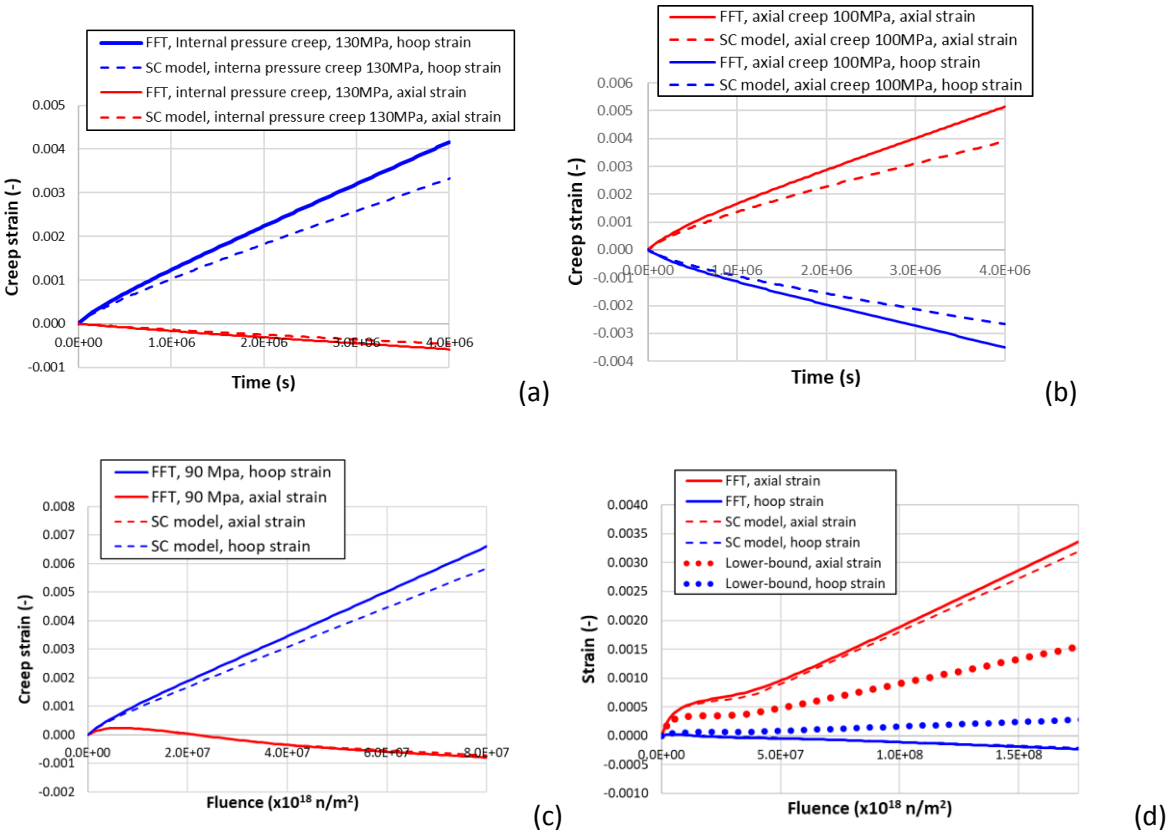

Figure 13: Simulations done with the self-consistent model compared with the FFT simulations (using Voronoi grains with N=21 and r=5). (a) internal pressure thermal creep test with 130 MPa hoop stress, (b) axial thermal creep test with 100 MPa axial stress, (c) internal pressure in-reactor creep test with 90 MPa hoop stress, (d) in-reactor growth test. On (d) the growth strains obtained with the lower-bound model are also shown.

The same comparison can be done by comparing the simulated hoop creep strain for the internal pressure test under irradiation with 90 MPa hoop stress and the axial growth strain. The creep strain simulated by the self-consistent model is 12% lower (for a fluence of φt=8×10^{25} n.m^{-2}) than the strain obtained from FFT simulations. When considering growth, the axial strain is only 5% lower (for a fluence of φt=1.75×10^{26} n.m^{-2}) than the strain simulated with the FFT tool.

The fact that the self-consistent model predicts lower strain values than the FFT simulations can be explained by the non-linearity of the thermal creep constitutive law. The self-consistent model requires the linearization of the non-linear constitutive law. This linearization is done using the affine procedure. It has been shown by Lebensohn et al. (Lebensohn et al., 2004) that linearizing the non-linear constitutive law using the secant, tangent or even the affine procedure amounts to neglect the intra-phase heterogeneity. This then leads to a too stiff model. On the other hand, by using the FFT numerical tool, the intraphase heterogeneity is taken into account since many grains with similar orientations are considered and furthermore, inside each grains, various voxels are considered. This thus induces a softer response.

For creep and growth tests under irradiation, the discrepancies between the self-consistent model and the FFT simulations are lower. This can be explained by a lower contribution of the non-linear thermal creep. To confirm this, the same simulations have been conducted without the non-linear thermal creep (using *ad-hoc* high reference resolved shear stresses).

For irradiation creep (Figure 14a) the discrepancy is now of only 2% (for a fluence of φt=8×10^{25} n.m^{-2}), which is remarkable considering the two very different homogenization methods, the difference in the crystallographic orientation file, the influence of the grain shape and also all the possible numerical errors associated with each method. This discrepancy decreases below 1% when exactly the same orientation file is used for both calculations.

Concerning growth (Figure 14b), the discrepancy between the self-consistent model and the FFT simulation remains equal to 4% without thermal creep (for a fluence of φt=1.75×10^{26} n.m^{-2}).

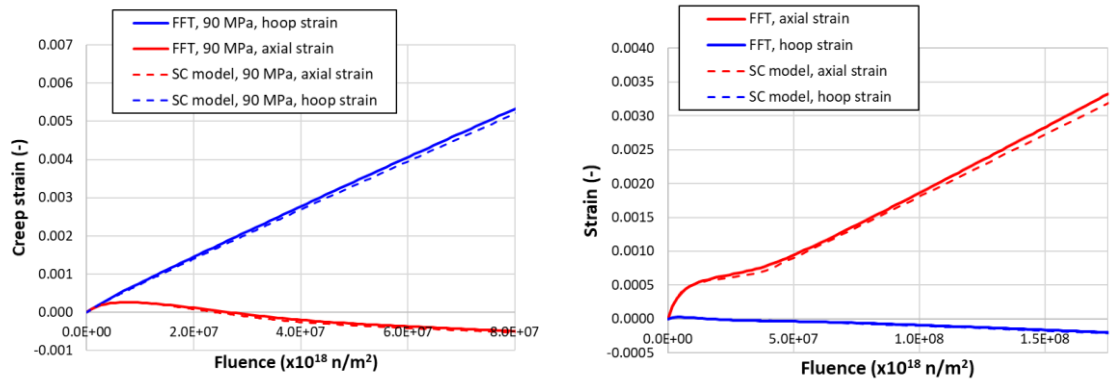

Figure 14: Self-consistent model and FFT simulations without thermal creep for (a) the in-reactor creep test (internal pressure) under irradiation with 90 MPa hoop stress and (b) irradiation induced growth test. FFT simulations conducted with *N*=21 and *r*=5 (continuous lines), and Self-consistent model, with 2527 orientations (dotted lines), are compared.

8. Discussions

8.1 Discussion on the importance of thermal creep during in-reactor deformation

By comparing the FFT simulations with and without thermal creep, it is possible to evaluate the contribution of thermal creep during in-reactor creep test. At 350°C and under an internal pressure leading to 90 MPa applied hoop stress, the thermal creep strain is equal to 19% of the overall creep strain (for a fluence of φt=8×10^{25} n.m^{-2}). However, because of the non-linear evolution with stress of thermal creep, this proportion increases as the stress increases. For an applied hoop stress of 120 MPa, the contribution of thermal creep becomes equal to 46% (for a fluence of φt=1.4×10^{25} n.m^{-2}). This analysis shows that although the contribution of thermal creep is generally considered to be small in-reactor, its contribution must not be neglected when the stress increases up to 120 MPa. On the other hand during growth test, the contribution of thermal creep is negligible.

8.2 Comparison between the simulated growth strain and the lower-bound model

It is interesting to compare the simulated growth strain with the classical approach based on the Kearns factors which is also called the lower-bound model. The lower bound model assumes homogeneous stress in the polycrystal. In the case of stress free growth (zero macroscopic applied stress), the local stress is equal to zero for each grain. Each grain behaves as an independent single crystal and the macroscopic strain is just the average of the strain in each grain (or each crystallographic phase). Because growth is considered to occur with constant volume, it can be shown that the macroscopic growth strain ($\overline{\varepsilon_{ii}}$) along the direction i is:

$$\overline{\varepsilon}_{ii} = (3F_i - 1)\frac{\varepsilon_c^{Growth}}{2} = (1 - 3F_i)\frac{q}{2} = (1 - 3F_i)\varepsilon_a^{Growth} \#(24)$$

Where ε_c is the growth strain along the <c>-axis, ε_a^{Growth} is the growth strain along the <c>-axis ($\varepsilon_c^{Growth} = -2\varepsilon_a^{Growth}$) and F_i is the Kearns factor along i which describes the resolved volume fraction of basal poles along the direction i (Adamson et al., 2019; Fong, 2013; Griffiths, 2020; Gruber et al., 2011; Kearns, 2014; Kocks et al., 1998; Murty and Charit, 2006). More details concerning the lower-bound model and the Kearns factor are given in Appendix B. The growth strain along the axial direction of the tube can then be calculated by using the appropriate Kearns factor (F_{1_ref}=0.103) and the strain evolution along the <c> axis. This calculation is compared with FFT and self-consistent model simulations on Fig. 13.

It can be seen on Fig. 13 that using the lower-bound model, the axial growth strain is more than 51% lower (for a fluence of φt=1.75×10^{26} n.m^{-2}) than the axial growth strain computed by the FFT simulations or the self-consistent model. The lower bound model thus significantly underestimates the axial growth strain. This shows that it is necessary to use a polycrystalline model to compute adequately the growth strain. This is particularly true when we want to introduce at the local scale, some microstructural internal variables, such as the <c> loop density, such that these quantities are consistent with TEM observations.

The fact that the growth strain computed by the FFT simulations is higher than the lower bound model shows the importance of the viscous interactions between grains during growth and thus the occurrence of irradiation creep at the local scale. As shown by Tomé et al. (Tomé et al., 1993) the effective macroscopic growth rate depends on both the crystallographic texture of the polycrystal and also, to a lesser extent, on the local anisotropic viscous behavior. With the crystallographic texture chosen and also the irradiation creep compliance chosen, the macroscopic growth strain rate along the axial direction is higher than with the lower-bound model. This is consistent with the early results published by Turner and Tomé (Turner and Tomé, 1993) although this point was not emphasized in this previous work.

It is worth mentioning that we have checked that, using exactly the same coefficients and the same constitutive equations as the ones used in (Turner and Tomé, 1993) and also using a very similar texture file, a good agreement is obtained between our simulation and the results obtained by Turner and Tomé (Turner and Tomé, 1993).

8.4 Discussion on the role of irradiation creep on stress free growth

The previous simulations show that there is an effect of the irradiation creep behavior on the stress free growth, as it was pointed out in the early study by Woo (Woo, 1985). As stated by Woo, “if the creep compliance of two specimens differ, their steady state growth behaviors will defer, even if the growth mechanism is the same”. In other words, if an alloy exhibits a high irradiation creep resistance, the growth strain should be lower, even with the same amount of <c> loops created under irradiation. In order to study this effect, the growth behavior has been computed with a lower irradiation creep rate. This is achieved by reducing the coefficient C_4 by a factor of 10. The new coefficient is C'_4=0.035. However, the thermal creep can still be activated in this simulation. The stationary axial growth rate is 16% lower than the reference growth strain. From this computation, it can be noticed that there is only a moderate effect of the irradiation creep resistance on irradiation growth.

8.5 Discussion on the correlation between <c>-loop microstructure and growth strain

There has been very few attempts to correlate quantitatively the macroscopic growth strain and the <c>-loop microstructure. The most extensive work is reported by Yagnik et al. (Yagnik et al., 2018) where the average <c>-loop linear density (L_c in m^{-2}) is plotted as a function of the macroscopic irradiation induced growth strain along the axial direction ($\overline{\varepsilon}_1$) for various alloys irradiated up to high doses. All these alloys have a Kearns factor along the axial direction (F_1) close to 0.1. For low <c>-loop density, below 10^{14} m^{-2} a linear correlation is noticed ($\overline{\varepsilon}_1 = K_c L_c$) with a proportionality coefficient close to 5×10^{-17} m^2. From our simulation, and neglecting the transient and stationary growth strain, this proportionality coefficient is found to be equal to 2.3×10^{-17} m^2 for a fluence of 1.5×10^{26} $n.m^{-2}$. This shows that there is a correct agreement between the data used in our model and the correlation found in the results provided by (Yagnik et al., 2018). For <c>-loop density higher than 10^{14} m^{-2} the proportionality coefficient progressively increases in the plot given by Yagnik et al. (Yagnik et al., 2018), showing a non-linear behavior. This is explained by the increase in <c>-loop diameter that cut the surfaces of the thin foil, in agreement with Eq. 21. Furthermore, when the loop is large enough to cut both surfaces, the loop contrast may be divided into two segments which further explains the progressive increase of the proportionality coefficient K_c with dose observed in (Yagnik et al., 2018). The coalescence of loops as they may also affect this proportionality coefficient. This shows that in order to simulate high dose irradiation growth, it is required, in future prospect, to take into account the fact that the loop contrast may be divided into two segments and the fact that the <c>-loop diameter increases with irradiation dose.

Conclusion

This study is a continuation of the long lasting effort to model in-reactor behavior of zirconium alloys. First, constitutive equations have been proposed to describe thermal creep and especially irradiation effect on thermal creep. Irradiation creep has been accounted for in a simple way following earlier works. An original approach is proposed to take into account the contribution of vacancy <c> component loops on the accelerated growth strain. These constitutive equations have been introduced into two homogenization models: Fast-Fourier Transform simulations and a self-consistent polycrystalline model. This was done to simulate an experimental data base obtained on recrystallized Zy-4 thin tubes during out-of-reactor and in-reactor tests.

Fast Fourier transform simulations on large grain aggregates have been applied for the first time to in-reactor deformation of zirconium alloys. A good description of thermal creep, in-reactor creep and in-reactor growth is obtained with microstructural inputs consistent with microscopic observations, such as <a> and <c> loop microstructures. These reference simulations have been compared with the self-consistent polycrystalline model. There is a good agreement between the two approaches when the behavior is linear with stress. For non-linear behavior, the affine self-consistent model is no more in agreement with FFT simulations. The FFT simulations have also been compared to the lower bound model which neglects interactions between grains. It is noticed that the lower-bound model underestimates the growth strain rate. The underestimation of the growth strain rate by the lower-bound model is explained by the importance of the viscous interactions between grains during growth and thus the occurrence of irradiation creep at the local scale. This shows that it is necessary to use a polycrystalline model, which takes into account the irradiation creep at the grain scale, to compute adequately the growth strain from the measurement of the <c> loop density.

Acknowledgments

This work has been funded by the project GAINE from the French nuclear tripartite institute CEA EDF Framatome.

Appendix A: Strain and stress distribution computed by FFT simulations

In this study, FFT simulations are used to deduce the macroscopic response of a large grain aggregate. However, during these simulations the detailed stress and strain fields are computed and are not analyzed. In this Appendix, some stress and strain fields are shown to illustrate the heterogeneous distribution of these fields throughout the polycrystal.

On the Fig. A-1(a) and (b) are shown the total axial strain and the axial stress fields at the end of irradiation growth (for a fluence of 1.75×10^{26} n/m^2). The simulations have been done using the unit-cell with Voronoi grains (seed choice #1) with N=21 and r=5. The local minimum value for axial strain is -0.85% and the maximum value is 2%. By using a color scale going from -0.5% up to 2% the heterogeneous strain field is clearly observed. Concerning the axial stress field, the minimum value is -80 MPa and the maximum value is 200 MPa. Using a color scale going from -50 MPa up to 150 MPa, the heterogeneous stress field can be clearly observed.

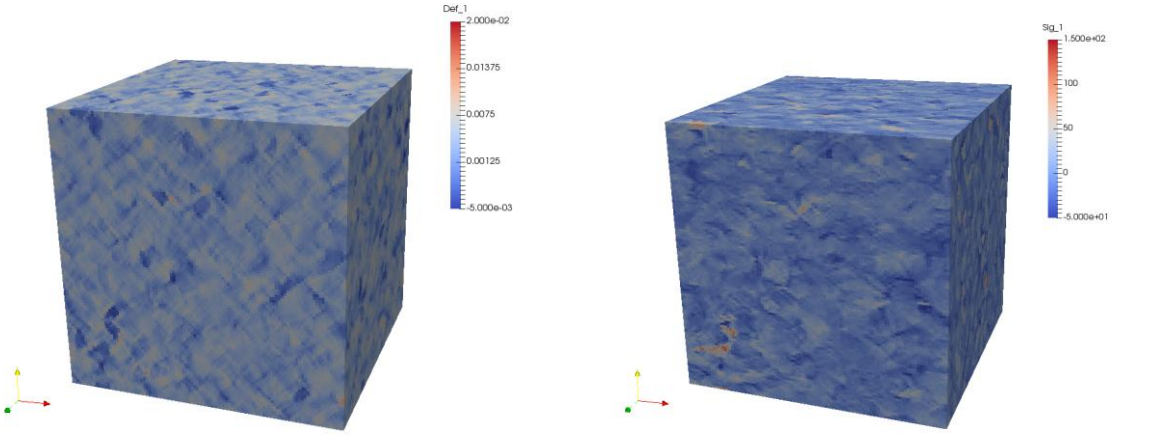

(a) **(b)**

Figure A-1: FFT simulation of the axial strain and axial stress distribution during irradiation induced growth.

On Fig. A-2(a) and (b) are shown the hoop strain and stress fields at the end of irradiation creep test (for a fluence of 8×10^{25} n/m^2). The creep test is conducted under biaxial stress condition, with a hoop stress of 90 MPa and an axial stress of 45 MPa. The local minimum value for hoop strain is -0.2% and the maximum value is 2.1%. By using a color scale going from 0% up to 2% the heterogeneous strain field is clearly observed. Concerning the axial stress field, the minimum value is -66 MPa and the maximum value is 260 MPa. Using a color scale going from -25 MPa up to 200 MPa, the heterogeneous stress field can be clearly observed.

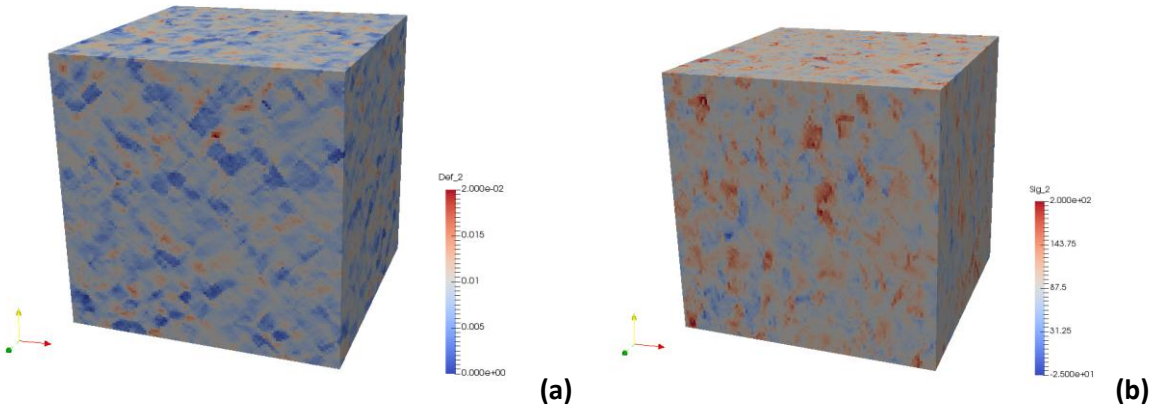

(a) (b)

Figure A-2: FFT simulation of the hoop strain and hoop stress distribution during irradiation creep test under biaxial stress condition, with a hoop stress of 90 MPa and an axial stress of 45 MPa.

Appendix B: Lower-bound model and Kearns factors

The lower-bound model, or Reuss model, assumes homogeneous stress throughout the polycrystal. During stress free growth, no macroscopic stress is applied leading to a local zero stress in the frame of the lower-bound model. The local elastic strain is thus equal to zero everywhere in the polycrystal, furthermore no creep occurs at the local scale. Thus, the overall macroscopic strain is just the weighted average of all the local growth strain (Eq. B-1).

$$\underline{\underline{\bar{\varepsilon}}} = \sum_r f_r \underline{\underline{\varepsilon}}_r^{growth} \#(\text{B-1})$$

In Eq. B-1, $\underline{\underline{\bar{\varepsilon}}}$ is the macroscopic strain tensor, $\underline{\underline{\varepsilon}}_r^{growth}$ is the local growth strain tensor of the crystallographic phase, noted r, but written in the specimen frame and f_r is the volume fraction of the crystallographic phase r. In the crystal frame, the growth strain tensor is the same for every crystallographic phases and can be written as Eq. B-2, with $\varepsilon_c = -2\varepsilon_a$.

$$\underline{\underline{\varepsilon}}_{cryst}^{growth} = \begin{bmatrix} \varepsilon_a & 0 & 0 \\ 0 & \varepsilon_a & 0 \\ 0 & 0 & \varepsilon_c \end{bmatrix} \#(\text{B-2})$$

The growth strain tensor can be written in the specimen frame as a function of the growth strain in the crystal frame by using the Euler rotation matrix $\underline{\underline{R}}_r$, with angles $(\varphi_1, \Phi, \varphi_2)$ as Eq. B-2. The angle Φ corresponds to the angle between the c-axis and the direction Z (or 3) of the specimen frame.

$$\underline{\underline{\varepsilon}}_r^{growth} = {}^T\underline{\underline{R}}_r \underline{\underline{\varepsilon}}_{cryst}^{growth} \underline{\underline{R}}_r \#(\text{B-3})$$

Using the usual Euler rotation matrix, the strain component along the Z-axis for each crystallographic phase can easily be computed as Eq. B-4.

$$\left(\varepsilon_r^{growth}\right)_{ZZ} = \varepsilon_a sin^2\Phi_r + \varepsilon_c cos^2\Phi_r \#(\text{B-4})$$

The macroscopic strain, averaged over the polycrystal, along the Z-axis is thus given by Eq. B-5, since the volume fraction of crystallographic phases is normalized to one.

$$\overline{\varepsilon}_{ZZ} = \sum_r f_r \left(\varepsilon_r^{growth}\right)_{ZZ} = \varepsilon_a + (\varepsilon_c - \varepsilon_a) F_Z \#(\text{B-5})$$

In Eq. B-5, F_Z corresponds to the Kearns factor along the Z-direction. It is computed as Eq. B-6.

$$F_Z = \sum_r f_r \, cos^2 \Phi_r \#(\text{B-6})$$

Using the fact that $\varepsilon_c = -2\varepsilon_a$ for growth strain, we obtain the classical relationship given in Eq. B-7.

$$\overline{\varepsilon}_{ZZ} = \varepsilon_a (1 - 3F_Z) \#(\text{B-7})$$

The Kearns texture factors are very useful, and thus widely used, to simply characterize the crystallographic texture of hexagonal polycrystals. These factors describe the effective volume fraction of crystallites with the basal pole aligned along three orthogonal sample directions, usually Rolling Direction (RD), Transverse Direction (TD) and Normal Direction (ND) for plates, with $F_{RD} + F_{TD} + F_{ND} = 1$.

Appendix C: Relationship between <c> loop number density and mean diameter and the <c> loops as observed edge-on by TEM.

TEM observations of <c> component loops are usually done using the diffraction vector g=0002. In these conditions, all the numerous <a>-loops are invisible, leading to an easy observation of <c>-loops. Because of the limited tilt angle in the TEM, this means that the <c>-axis of the analyzed grain is close to the thin foil plane. Because the <c>-loop habit plane is the basal plane, the <c>-loops are thus observed edge-on. The foil thickness needed for conventional TEM observations is small, usually around 150 nm depending on the material and on the objects analyzed. If the loops are small enough they are fully contained in the thin foil and the mean loop diameter and density can be accurately characterized. Only few loops, close to the surface may be cut. However, when the loops are large they are cut by the surfaces of the thin foil. Using a simple geometrical analysis, we have derived the formula which gives the mean length of the intersection between the loop plane, for a loop population with mean diameter d_c and a thin foil of thickness t.

Let's consider a loop population with the same diameter d_c or radius R ($d_c = 2R$) (Hypothesis 1) and a thin foil of thickness t. The loop centre can be located, with equal probability, at various height (z) with respect to the middle of the foil. Let's consider that the loop habit plane is perpendicular to the surfaces of the thin foil (hypothesis 2). The upper surface of the thin foil is located at z=0, the middle of the thin foil is located at $z = -t/2$. Let's first consider a single loop. The center of the <c> loop is located at the elevation z. Only loops with $z \geq -t/2$ are considered since the system is symmetric with respect to the middle of the foil. The maximum length, $L(z)$, of the intersection between the loop plane and the foil, which is what is observed by TEM, for all possible locations of the loop centre with respect to the foil can be calculated. In this approach, it is assumed that the loop plane can always be observed, even when the loop is cut by the two surfaces (hypothesis 3). This is a strong assumption since in that case only the stacking fault is present between the two surfaces. It is thus possible that the resulting contrast leads to the observation of only two segments on both sides of the loop. This would decrease further the apparent dislocation length in the thin foil, compared to the real dislocation loop diameter. More investigations are needed to elucidate this point.

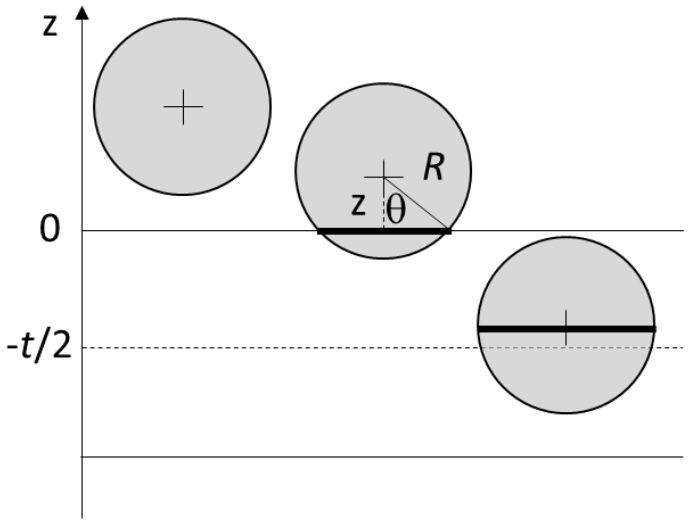

Figure C-1: Schematic showing the maximum length of the intersection between the loop plane and the foil.

For $z > R$ then $L(z) = 0$

For $0 \leq z \leq R$ then $L(z) = 2R\sin(\theta)$, with θ the angle between the z-axis and the radius shown on Fig. C-1.

For $-t/2 \leq z \leq 0$ then $L(z) = 2R$

The average of this maximum length, $< L >$, can be computed by considering only the upper half of the thin foil thickness. The average of the maximum length of the intersection between the loop plane and the foil is thus equal to:

$$\langle L \rangle = \frac{1}{R + \frac{t}{2}} \int_{-\frac{t}{2}}^{R} L(z)dz = \frac{1}{R + \frac{t}{2}} \left(\int_{-\frac{t}{2}}^{0} L(z)dz + \int_{0}^{R} L(z)dz \right) = \frac{1}{R + \frac{t}{2}} \left(Rt + \frac{\pi R^2}{2} \right) \#(\text{C-1})$$

By replacing $d_c = 2R$, we obtain:

$$\langle L \rangle = \frac{d_c}{d_c + t} \left(t + \frac{\pi d_c}{4} \right) \#(\text{C-2})$$

Knowing the loop number density of loops, N_c, the number of loops intersecting the thin foil can be calculated as $N_c(d_c + t)S$. Then the quantity L_c can be computed according to its definition, given in Eq. 18

$$L_c = \frac{1}{tS} \sum l_i = \frac{1}{tS} N_c(d_c + t)S\langle L \rangle = N_c \frac{d_c}{t} \left(t + \frac{\pi d_c}{4} \right) \#(\text{C-3})$$

From Eq. 20 and 21, it can be noticed that the strain along the c-axis ε_c is related to both the quantity L_c and the loop mean diameter d_c. By measuring only L_c it is not possible to deduce the strain along the c-axis. A measure of the loop mean diameter d_c is also needed. As reported in the core of this article, several authors show c-loops observed edge-on. However, very few authors show c-loops observed in the foil plane. In the following two pictures of the same material are given for c-loops observed edge-on (Fig. C-2(a)) or observed in the foil plane (Fig. C-2(b)). The material is a Zr-1%Nb-O recrystallized zirconium alloy irradiated in a PWR reactor. After irradiation the material has been annealed at 450°C during 40 days. From the “in-foil” picture (Fig. C-2(b)), it is noticed that c-loops

have diameters ranging from 130 nm up to 300 nm. The mean diameter being 220 nm. The c-loops are not very sensitive to annealing and have probably not significantly evolved compared with as irradiated samples.

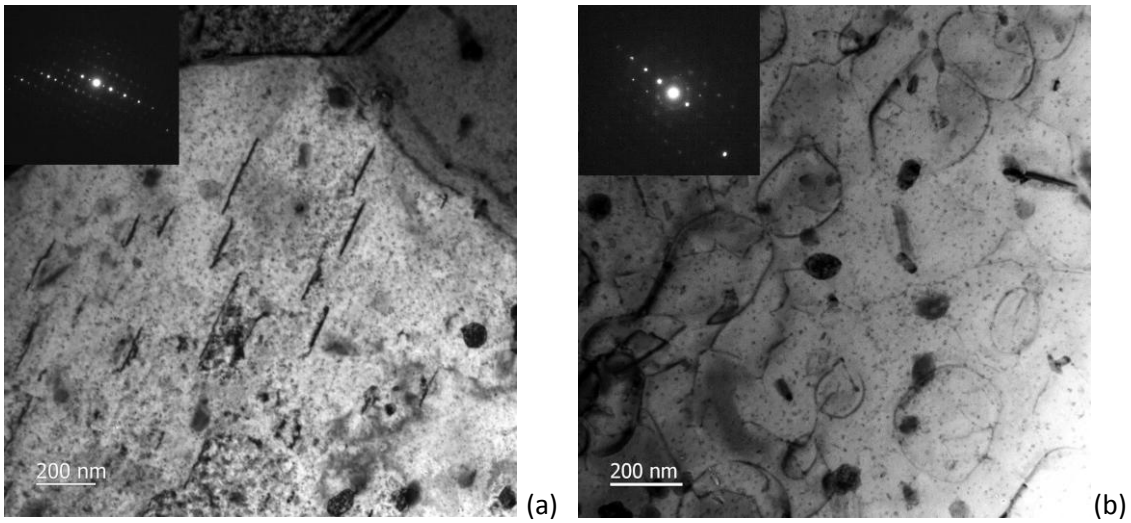

(a) (b)

Figure C-2: (a) c-loops observed “edge-on” with diffraction vector g=0002, (b) c-loops observed “in-foil” with diffraction vector g= $01\bar{1}1$.

References

Adamson, R.B., Coleman, C.E., Griffiths, M., 2019. Irradiation creep and growth of zirconium alloys: A critical review. J. Nucl. Mater. 521, 167–244. https://doi.org/10.1016/j.jnucmat.2019.04.021

Allen, T.R., Konings, R.J.M., Motta, A.T., Couet, A., 2020. Corrosion of Zirconium Alloys, in: Comprehensive Nuclear Materials, Second Edition. Elsevier Ltd, pp. 64–95.

AMITEX software, n.d.

Barashev, A.V., Golubov, S.I., Stoller, R.E., 2015. Theoretical investigation of microstructure evolution and deformation of zirconium under neutron irradiation. J. Nucl. Mater. 461, 85–94. https://doi.org/10.1016/j.jnucmat.2015.02.001

Barbe, F., Decker, L., Jeulin, D., Cailletaud, G., 2001. Intergranular and intragranular behavior of polycrystalline aggregates. Part 1: F.E. model. Int. J. Plast. 17, 513–536. https://doi.org/10.1016/s0749-6419(00)00061-9

Baron, J.L., Esling, C., Feron, J.L., Gex, D., Glimois, J.L., Guillen, R., Humbert, M., Lemoine, P., Lepape, J., Mardon, J.P., Thil, A., Uny, G., 1990. Interlaboratories Tests of Textures of Zircaloy-4 Tubes. Part 1: Pole Figure Measurements and Calculation of Kearns Coefficients. Textures Microstruct. 12, 125–140. https://doi.org/10.1155/tsm.12.125

Bossis, P., Verhaeghe, B., Doriot, S., Gilbon, D., Chabretou, V., Dalmais, A., Mardon, J.-P., Blat, M., Miquet, A., 2009. In PWR Comprehensive Study of High Burn-Up Corrosion and Growth Behavior of M5® and Recrystallized Low-Tin Zircaloy-4. Zircon. Nucl. Ind. 15th Int. Symp. ASTM STP 1505, 430–430. https://doi.org/10.1520/stp48148s

Brenner, R., Béchade, J.L., Castelnau, O., Bacroix, B., 2002a. Thermal creep of Zr–Nb1%–O alloys: experimental analysis and micromechanical modelling. J. Nucl. Mater. 305, 175–186. https://doi.org/10.1016/s0022-3115(02)00923-6

Brenner, R., Masson, R., Castelnau, O., Zaoui, A., 2002b. A “quasi-elastic” affine formulation for the homogenised behaviour of nonlinear viscoelastic polycrystals and composites. Eur. J. Mech. - ASolids 21, 943–960. https://doi.org/10.1016/s0997-7538(02)01247-0

Cailletaud, G., 1992. A micromechanical approach to inelastic behaviour of metals. Int. J. Plast. 8, 55–73. https://doi.org/10.1016/0749-6419(92)90038-e

Cailletaud, G., Pilvin, P., 1994. Utilisation de modèles polycristallins pour le calcul par éléments finis. Rev. Eur. Éléments Finis 3, 515–541. https://doi.org/10.1080/12506559.1994.10511147

Carpenter, G.J.C., Zee, R.H., Rogerson, A., 1988. Irradiation growth of zirconium single crystals: A review. J. Nucl. Mater. 159, 86–100. https://doi.org/10.1016/0022-3115(88)90087-6

Causey, A.R., Woo, C.H., Holt, R.A., 1988. The effect of intergranular stresses on the texture dependence of irradiation growth in zirconium alloys. J. Nucl. Mater. 159, 225–236. https://doi.org/10.1016/0022-3115(88)90095-5

Chen, Y., Gélébart, L., Chateau, C., Bornert, M., Sauder, C., King, A., 2019. Analysis of the damage initiation in a SiC/SiC composite tube from a direct comparison between large-scale numerical simulation and synchrotron X-ray micro-computed tomography. Int. J. Solids Struct. 161, 111–126. https://doi.org/10.1016/j.ijsolstr.2018.11.009

Cho, J.-H., Rollett, A.D., Oh, K.H., 2004. Determination of volume fractions of texture components with standard distributions in Euler space. Metall. Mater. Trans. A 35, 1075–1086. https://doi.org/10.1007/s11661-004-1010-y

Christien, F., Barbu, A., 2009. Cluster Dynamics modelling of irradiation growth of zirconium single crystals. J. Nucl. Mater. 393, 153–161. https://doi.org/10.1016/j.jnucmat.2009.05.016

Christodoulou, N., Causey, A., Holt, R., Tomé, C., Badie, N., Klassen, R., Sauvé, R., Woo, C., 1996. Modeling In-Reactor Deformation of Zr-2.5Nb Pressure Tubes in CANDU Power Reactors. Zircon. Nucl. Ind. Elev. Int. Symp., ASTM International ASTM STP 1295, 518–537. https://doi.org/10.1520/stp16188s

Delannay, L., Jacques, P.J., Kalidindi, S.R., 2006. Finite element modeling of crystal plasticity with grains shaped as truncated octahedrons. Int. J. Plast. 22, 1879–1898. https://doi.org/10.1016/j.ijplas.2006.01.008

Diard, O., Leclercq, S., Rousselier, G., Cailletaud, G., 2005. Evaluation of finite element based analysis of 3D multicrystalline aggregates plasticity. Int. J. Plast. 21, 691–722. https://doi.org/10.1016/j.ijplas.2004.05.017

Doriot, S., Verhaeghe, B., Béchade, J.-L., Menut, D., Gilbon, D., Mardon, J.-P., Cloué, J.-M., Miquet, A., Legras, L., 2014. Microstructural Evolution of M5 Alloy Irradiated in PWRs up to High Fluences—Comparison With Other Zr-Based Alloys. Zircon. Nucl. Ind. 17th Vol. ASTM STP 1543, 759–799. https://doi.org/10.1520/stp154320120179

Doriot, S., Verhaeghe, B., Soniak-Defresne, A., Bossis, P., Gilbon, D., Chabretou, V., Mardon, J.-P., Ton-That, M., Ambard, A., 2018. Microstructural Evolution of Q12TM Alloy Irradiated in PWRs and Comparison with Other Zr Base Alloys. Zircon. Nucl. Ind. 18th Int. Symp. ASTM STP 1597, 823–856. https://doi.org/10.1520/stp159720160061

Erinosho, T.O., Dunne, F.P.E., 2015. Strain localization and failure in irradiated zircaloy with crystal plasticity. Int. J. Plast. 71, 170–194. https://doi.org/10.1016/j.ijplas.2015.05.008

Fidleris, V., 1988. The irradiation creep and growth phenomena. J. Nucl. Mater. 159, 22–42. https://doi.org/10.1016/0022-3115(88)90083-9

Fisher, E.S., Renken, C.J., 1964. Single-Crystal Elastic Moduli and the hcp → bcc Transformation in Ti, Zr, and Hf. Phys. Rev. 135, A482–A494. https://doi.org/10.1103/physrev.135.a482

Fong, R.W.L., 2013. Anisotropy factors from texture and mechanical strain in Zircaloy-4 fuel sheaths. J. Nucl. Mater. 440, 288–297. https://doi.org/10.1016/j.jnucmat.2013.04.089

Franklin, D.G., Adamson, R.B., 1988. Implications of Zircaloy creep and growth to light water reactor performance. J. Nucl. Mater. 159, 12–21. https://doi.org/10.1016/0022-3115(88)90082-7

Garzarolli, F., Dewes, P., Maussner, G., Basso, H.-H., 1989. Effects of High Neutron Fluences on Microstructure and Growth of Zircaloy-4. Zircon. Nucl. Ind. Eighth Int. Symp., ASTM International ASTM STP 1023, 641–657. https://doi.org/10.1520/stp18891s

Gélébart, L., 2020. A modified FFT-based solver for the mechanical simulation of heterogeneous materials with Dirichlet boundary conditions. Comptes Rendus Mécanique 348, 693–704. https://doi.org/10.5802/crmeca.54

Gélébart, L., Mondon-Cancel, R., 2013. Non-linear extension of FFT-based methods accelerated by conjugate gradients to evaluate the mechanical behavior of composite materials. Comput. Mater. Sci. 77, 430–439. https://doi.org/10.1016/j.commatsci.2013.04.046

Gélébart, L., Ouaki, F., 2015. Filtering material properties to improve FFT-based methods for numerical homogenization. J. Comput. Phys. 294, 90–95. https://doi.org/10.1016/j.jcp.2015.03.048

Gilbon, D., Soniak, A., Doriot, S., Mardon, J.-P., 2000. Irradiation Creep and Growth Behavior, and Microstructural Evolution of Advanced Zr-Base Alloys. Zircon. Nucl. Ind. Twelfth Int. Symp. ASTM STP 1354, 51–73. https://doi.org/10.1520/stp14294s

Griffiths, M., 2020. Irradiation Growth, in: Comprehensive Nuclear Materials, Second Edition. Elsevier Ltd, pp. 367–405.

Griffiths, M., Gilbert, R., Fidleris, V., 1989. Accelerated Irradiation Growth of Zirconium Alloys. Zircon. Nucl. Ind. Eighth Int. Symp., ASTM International ASTM STP 1023, 658–677. https://doi.org/10.1520/stp18892s

Griffiths, M., Holt, R.A., Rogerson, A., 1995. Microstructural aspects of accelerated deformation of Zircaloy nuclear reactor components during service. J. Nucl. Mater. 225, 245–258. https://doi.org/10.1016/0022-3115(94)00687-3

Gruber, J.A., Brown, S.A., Lucadamo, G.A., 2011. Generalized Kearns texture factors and orientation texture measurement. J. Nucl. Mater. 408, 176–182. https://doi.org/10.1016/j.jnucmat.2010.11.031

Harte, A., Jädernäs, D., Topping, M., Frankel, P., Race, C.P., Romero, J., Hallstadius, L., Darby, E.C., Preuss, M., 2017. The effect of matrix chemistry on dislocation evolution in an irradiated Zr alloy. Acta Mater. 130, 69–82. https://doi.org/10.1016/j.actamat.2017.03.024

Holt, R.A., 2008. In-Reactor Deformation of Zirconium Alloy Components. J. ASTM Int., ASTM STP 5, 101354. https://doi.org/10.1520/jai101354

Holt, R.A., Causey, A.R., 2004. Volume conservation during irradiation growth of Zr–2.5Nb. J. Nucl. Mater. 335, 529–533. https://doi.org/10.1016/j.jnucmat.2004.07.042
Holt, R.A., Gilbert, R.W., 1986. c-Component dislocations in annealed Zircaloy irradiated at about 570 K. J. Nucl. Mater. 137, 185–189. https://doi.org/10.1016/0022-3115(86)90218-7
Huet, C., 1990. Application of variational concepts to size effects in elastic heterogeneous bodies. J. Mech. Phys. Solids 38, 813–841. https://doi.org/10.1016/0022-5096(90)90041-2
Kanit, T., Forest, S., Galliet, I., Mounoury, V., Jeulin, D., 2003. Determination of the size of the representative volume element for random composites: statistical and numerical approach. Int. J. Solids Struct. 40, 3647–3679. https://doi.org/10.1016/s0020-7683(03)00143-4
Kearns, J.J., 2014. Reflections on the Development of the "f" Texture Factors for Zirconium Components and the Establishment of Properties of the Zirconium–Hydrogen System. Zircon. Nucl. Ind. 17th Vol. 3–22. https://doi.org/10.1520/stp154320120216
Kocks, U.F., Tomé, C.N., Wenk, H.-R., 1998. Texture and anisotropy: preferred orientations in polycrystals and their effect on materials properties. Cambridge university press.
LABOTEX software, n.d.
Lebensohn, R.A., Castelnau, O., Brenner, R., Gilormini, P., 2005. Study of the antiplane deformation of linear 2-D polycrystals with different microstructures. Int. J. Solids Struct. 42, 5441–5459. https://doi.org/10.1016/j.ijsolstr.2005.02.051
Lebensohn, R.A., Kanjarla, A.K., Eisenlohr, P., 2012. An elasto-viscoplastic formulation based on fast Fourier transforms for the prediction of micromechanical fields in polycrystalline materials. Int. J. Plast. 32–33, 59–69. https://doi.org/10.1016/j.ijplas.2011.12.005
Lebensohn, R.A., Liu, Y., Ponte Castañeda, P., 2004. On the accuracy of the self-consistent approximation for polycrystals: comparison with full-field numerical simulations. Acta Mater. 52, 5347–5361. https://doi.org/10.1016/j.actamat.2004.07.040
Lebensohn, R.A., Tomé, C.N., 1993. A self-consistent anisotropic approach for the simulation of plastic deformation and texture development of polycrystals: Application to zirconium alloys. Acta Metall. Mater. 41, 2611–2624. https://doi.org/10.1016/0956-7151(93)90130-k
Limbäck, M., Andersson, T., 1996. A Model for Analysis of the Effect of Final Annealing on the In- and Out-of-Reactor Creep Behavior of Zircaloy Cladding. Zircon. Nucl. Ind. Elev. Int. Symp. ASTM STP 1295, 448–448. https://doi.org/10.1520/stp16185s
Marano, A., Gélébart, L., 2020. Non-linear composite voxels for FFT-based explicit modeling of slip bands: Application to basal channeling in irradiated Zr alloys. Int. J. Solids Struct. 198, 110–125. https://doi.org/10.1016/j.ijsolstr.2020.04.027
Marano, A., Gélébart, L., Forest, S., 2019. Intragranular localization induced by softening crystal plasticity: Analysis of slip and kink bands localization modes from high resolution FFT-simulations results. Acta Mater. 175, 262–275. https://doi.org/10.1016/j.actamat.2019.06.010
Masson, R., Bornert, M., Suquet, P., Zaoui, A., 2000. An affine formulation for the prediction of the effective properties of nonlinear composites and polycrystals. J. Mech. Phys. Solids 48, 1203–1227. https://doi.org/10.1016/s0022-5096(99)00071-x
Masson, R., Zaoui, A., 1999. Self-consistent estimates for the rate-dependentelastoplastic behaviour of polycrystalline materials. J. Mech. Phys. Solids 47, 1543–1568. https://doi.org/10.1016/s0022-5096(98)00106-9
Michel, J.C., Moulinec, H., Suquet, P., 2001. A computational scheme for linear and non-linear composites with arbitrary phase contrast. Int. J. Numer. Methods Eng. 52, 139–160. https://doi.org/10.1002/nme.275
Montgomery, R., Tomé, C., Liu, W., Alankar, A., Subramanian, G., Stanek, C., 2017. Use of multiscale zirconium alloy deformation models in nuclear fuel behavior analysis. J. Comput. Phys. 328, 278–300. https://doi.org/10.1016/j.jcp.2016.09.051
Moulinec, H., Suquet, P., 1998. A numerical method for computing the overall response of nonlinear composites with complex microstructure. Comput. Methods Appl. Mech. Eng. 157, 69–94. https://doi.org/10.1016/s0045-7825(97)00218-1

Murty, K.L., Charit, I., 2006. Texture development and anisotropic deformation of zircaloys. Prog. Nucl. Energy 48, 325–359. https://doi.org/10.1016/j.pnucene.2005.09.011
Nagra, J.S., Brahme, A., Lebensohn, R.A., Inal, K., 2017. Efficient fast Fourier transform-based numerical implementation to simulate large strain behavior of polycrystalline materials. Int. J. Plast. 98, 65–82. https://doi.org/10.1016/j.ijplas.2017.07.001
Northwood, D., 1977. Irradiation damage in zirconium and its alloys. At. Energy Rev. 15, 547–610.
Onimus, F., Béchade, J.-L., 2009. A polycrystalline modeling of the mechanical behavior of neutron irradiated zirconium alloys. J. Nucl. Mater. 384, 163–174. https://doi.org/10.1016/j.jnucmat.2008.11.006
Onimus, F., Bono, M., Verhaeghe, B., Soniak, A., Pilvin, P., 2020a. Polycrystalline modeling of the behavior of neutron-irradiated recrystallized zirconium alloys during strain path change tests. Int. J. Plast. 134, 102835. https://doi.org/10.1016/j.ijplas.2020.102835
Onimus, F., Doriot, S., Béchade, J.-L., 2020b. Radiation Effects in Zirconium Alloys, Konings, R., Stoller, R. E. Eds. ed, Comprehensive Nuclear Materials, Second Edition. Elsevier Ltd.
Onimus, F., Jourdan, T., Xu, C., Campbell, A.A., Griffiths, M., 2020c. Irradiation Creep in Materials, Konings, R., Stoller, R. E. Eds. ed, Comprehensive Nuclear Materials, Second Edition. Elsevier Ltd.
Paramatmuni, C., Kanjarla, A.K., 2019. A crystal plasticity FFT based study of deformation twinning, anisotropy and micromechanics in HCP materials: Application to AZ31 alloy. Int. J. Plast. 113, 269–290. https://doi.org/10.1016/j.ijplas.2018.10.007
Patra, A., Tomé, C.N., Golubov, S.I., 2017. Crystal plasticity modeling of irradiation growth in Zircaloy-2. Philos. Mag. 97, 2018–2051. https://doi.org/10.1080/14786435.2017.1324648
Pawlik, K., 1986. Determination of the orientation distribution function from pole figures in arbitrarily defined cells. Phys. Status Solidi B 134, 477–483. https://doi.org/10.1002/pssb.2221340205
Raabe, D., Sachtleber, M., Zhao, Z., Roters, F., Zaefferer, S., 2001. Micromechanical and macromechanical effects in grain scale polycrystal plasticity experimentation and simulation. Acta Mater. 49, 3433–3441. https://doi.org/10.1016/s1359-6454(01)00242-7
Rogerson, A., 1988. Irradiation growth in zirconium and its alloys. J. Nucl. Mater. 159, 43–61. https://doi.org/10.1016/0022-3115(88)90084-0
Roters, F., Eisenlohr, P., Hantcherli, L., Tjahjanto, D.D., Bieler, T.R., Raabe, D., 2010. Overview of constitutive laws, kinematics, homogenization and multiscale methods in crystal plasticity finite-element modeling: Theory, experiments, applications. Acta Mater. 58, 1152–1211. https://doi.org/10.1016/j.actamat.2009.10.058
Schneider, M., Merkert, D., Kabel, M., 2016. FFT-based homogenization for microstructures discretized by linear hexahedral elements. Int. J. Numer. Methods Eng. 109, 1461–1489. https://doi.org/10.1002/nme.5336
Soniak, A., L'Hullier, N., Mardon, J.-P., Rebeyrolle, V., Bouffioux, P., Bernaudat, C., 2002. Irradiation Creep Behavior of Zr-Base Alloys. Zircon. Nucl. Ind. Thirteen. Int. Symp. ASTM STP 1423, 837–862. https://doi.org/10.1520/stp11419s
Tewari, R., Mani Krishna, K.V., Neogy, S., Lemaignan, C., 2020. Zirconium and its Alloys: Properties and Characteristics, in: Comprehensive Nuclear Materials, Second Edition. Elsevier Ltd, pp. 284–302.
Tomé, C.N., Christodoulou, N., 2000. Analysis of accelerated irradiation growth in Zr-2.5% Nb pressure tubes. Philos. Mag. A 80, 1407–1424. https://doi.org/10.1080/01418610008212127
Tomé, C.N., Christodoulou, N., Turner, P.A., Miller, M.A., Woo, C.H., Root, J., Holden, T.M., 1996. Role of internal stresses in the transient of irradiation growth of Zircaloy-2. J. Nucl. Mater. 227, 237–250. https://doi.org/10.1016/0022-3115(95)00140-9
Tomé, C.N., So, C.B., Woo, C.H., 1993. Self-consistent calculation of steady-state creep and growth in textured zirconium. Philos. Mag. A 67, 917–930. https://doi.org/10.1080/01418619308213968
Tromans, D., 2011. Elastic anisotropy of HCP metal crystals and polycrystals. Int. J. Res. Rev. Appl. Sci. 6, 462–483.

Turner, P.A., Tomé, C.N., 1993. Self-consistent modeling of visco-elastic polycrystals: Application to irradiation creep and growth. J. Mech. Phys. Solids 41, 1191–1211. https://doi.org/10.1016/0022-5096(93)90090-3

Turner, P.A., Tomé, C.N., Christodoulou, N., Woo, C.H., 1999. A self-consistent model for polycrystals undergoing simultaneous irradiation and thermal creep. Philos. Mag. A 79, 2505–2524. https://doi.org/10.1080/01418619908214296

Turner, P.A., Tomé, C.N., Woo, C.H., 1994. Self-consistent modelling of nonlinear visco-elastic polycrystals: An approximate scheme. Philos. Mag. A 70, 689–711. https://doi.org/10.1080/01418619408242256

Willot, F., 2015. Fourier-based schemes for computing the mechanical response of composites with accurate local fields. Comptes Rendus Mécanique 343, 232–245. https://doi.org/10.1016/j.crme.2014.12.005

Woo, C.H., 1988. Theory of irradiation deformation in non-cubic metals: Effects of anisotropic diffusion. J. Nucl. Mater. 159, 237–256. https://doi.org/10.1016/0022-3115(88)90096-7

Woo, C.H., 1985. Polycrystalline effects on irradiation creep and growth in textured zirconium. J. Nucl. Mater. 131, 105–117. https://doi.org/10.1016/0022-3115(85)90449-0

Yagnik, S., Adamson, R., Kobylyansky, G., Chen, J.-H., Gilbon, D., Ishimoto, S., Fukuda, T., Hallstadius, L., Obukhov, A., Mahmood, S., 2018. Effect of Alloying Elements, Cold Work, and Hydrogen on the Irradiation-Induced Growth Behavior of Zirconium Alloy Variants. Zircon. Nucl. Ind. 18th Int. Symp. ASTM STP 1597, 748–795. https://doi.org/10.1520/stp159720160040